SANDIA REPORT

SAND2005-6454
Unlimited Release
Printed March 2006

Modal Testing of the TX-100 Wind Turbine Blade

D. Todd Griffith, Gregory Smith, Miguel Casias, Sarah Reese, and Todd W. Simmermacher

Prepared by
Sandia National Laboratories
Albuquerque, New Mexico 87185 and Livermore, California 94550

Sandia is a multiprogram laboratory operated by Sandia Corporation,
a Lockheed Martin Company, for the United States Department of Energy's
National Nuclear Security Administration under Contract DE-AC04-94AL85000.

Issued by Sandia National Laboratories, operated for the United States Department of Energy by Sandia Corporation.

Available to DOE and DOE contractors from
U.S. Department of Energy
Office of Scientific and Technical Information
P.O. Box 62
Oak Ridge, TN 37831

Telephone: (865) 576-8401
Facsimile: (865) 576-5728
E-Mail: reports@adonis.osti.gov
Online ordering: http://www.osti.gov/bridge

Available to the public from
U.S. Department of Commerce
National Technical Information Service
5285 Port Royal Rd.
Springfield, VA 22161

Telephone: (800) 553-6847
Facsimile: (703) 605-6900
E-Mail: orders@ntis.fedworld.gov
Online order: http://www.ntis.gov/help/ordermethods.asp?loc=7-4-0#online

SAND2005-6454
Unlimited Release
Printed May 2006

Modal Testing of the TX-100 Wind Turbine Blade

D. Todd Griffith
Structural Dynamics Research Department

Gregory Smith
Structural Dynamics Engineering Department

Miguel Casias
Structural Dynamics Engineering Department

Sarah Reese
Structural Dynamics Research Department

Todd W. Simmermacher
Structural Dynamics Research Department

Sandia National Laboratories
P.O. Box 5800
Albuquerque, New Mexico 87185-0557

Abstract

This test report covers the SNL modal test results for two nominally identical TX-100 wind turbine blades. The TX-100 blade design is unique in that it features a passive braking, force-shedding mechanism where bending and torsion are coupled to produce desirable aerodynamic characteristics. A specific aim of this test is to characterize the coupling between bending and torsional dynamics. The results of the modal tests and the subsequent analysis characterize the natural frequencies, damping, and mode shapes of the individual blades. The results of this report are expected to be used for model validation -- the frequencies and mode shapes from the experimental analysis can be compared with those of a finite-element analysis. Damping values are included in the results of these tests to potentially improve the fidelity of numerical simulations, although numerical finite element models typically have no means of predicting structural damping characteristics. Thereafter, an additional objective of the test is achieved in evaluating the test to test and unit variation in the modal parameters of the two blades.

Acknowledgments

The authors would like to thank Gerry Langwell (6252, Airworthiness Assurance Department) for his assistance in preparing the test space for these tests. We also acknowledge Colin Horvat (1525, Structural Dynamics Engineering Department) for his help with instrumentation. We also thank Tom Carne, Josh Paquette, and Mark Rumsey for reviewing drafts of this report.

Contents

Figures

Tables

Introduction and Motivation

The size of utility-grade wind turbine rotors continues to increase, especially for offshore applications. Designs of wind turbines with ratings of 3-5 MW are now being considered [1]. This growth in size puts pressure on blade designers to constrain the associated weight increases while maintaining acceptable tip deflections.

To address this challenge, the Sandia National Laboratories (SNL) Wind Energy Technology Department has initiated a *Carbon-Hybrid Blade Developments: Standard and Twist-Coupled Prototypes* project and a *Blade System Design Studies* project that seeks to design, model and fabricate 100-KW-sized, carbon-hybrid, 9-meter blades to study potential weight reductions and investigate ways to incorporate both epoxy-glass and carbon fiber in the blades in an efficient structural manner.

The projects have the goal of designing, modeling, manufacturing and testing a standard blade design, referred to as the carbon experimental or CX-100 blade; a twist-coupled experimental or TX-100 blade design; and an integration of advanced blade concepts into the BSDS blade design. Laboratory and field test results will be used to improve the blade design tools, the manufacturing process, and help validate the blade structural models.

This test report covers the SNL modal test results for two nominally identical TX-100 wind turbine blades. The TX-100 blade design is unique in that it features a passive braking, force-shedding mechanism where bending and torsion are coupled to produce desirable aerodynamic characteristics. A specific aim of this test is to characterize the coupling between bending and torsional dynamics. The results of the modal tests and the subsequent analysis characterize the natural frequencies, damping, and mode shapes of the individual blades. The results of this report are expected to be used for model validation -- the frequencies and mode shapes from the experimental analysis can be compared with those of a finite-element analysis. Damping values are included in the results of these tests to potentially improve the fidelity of numerical simulations, although numerical finite element models typically have no means of predicting structural damping characteristics. Thereafter, an additional objective of the test is achieved in evaluating the test to test and unit variation in the modal parameters of the two blades.

Test Setup and Instrumentation

A number of key factors were considered in the test setup. These include the method of suspending the blade for testing, protection of the blade surface, safety, environmental factors, instrumentation and mass loading effects. Each of these is described in this section. A photo of a fully instrumented blade sitting in the storage cradles is shown in Figure 1.

Figure 1. Fully Instrumented Wind Turbine Blade Sitting in Storage Cradles

The blade was tested in a free-free condition. The free boundary condition is preferred from a model validation point of view because it is the easiest to realize in practice and is thus a preferable configuration to perform a modal test for the purpose of model validation. Any other idealized constraint condition is, in practice, affected by the compliance of the system applying the constraint. For example, if the blade was tested while being mounted at the hub, the compliance of the mount would affect the results. This compliance, of course, would need to be characterized for the purpose of any model validation. Therefore, special care must be taken so that the suspension system will not have a noticeable influence on the test results. For these tests, the blade was suspended by bungee cords to approximate the free-free boundary condition.

The blades were tested in two configurations. In one configuration, the free-free boundary condition was approximated by suspending the blade at two locations using two independent tripods positioned fore and aft the blade's center of gravity (CG). At each location, the blade was supported by a single nylon strap which was linked to the tripod with a coil of bungee rope. A photo of the double strap suspension configuration is shown in Figure 2. In order to evaluate the suspension setup, tests were repeated for a different suspension configuration using only a single nylon strap and tripod positioned at the CG as shown in Figure 3. The differences between the single and double strap tests were minimal. Additionally, there was adequate frequency separation between modes related to the suspension and the first flexible mode. Suspension related modes include the bounce mode of the blade/bungee system and a roll/pendulum mode associated with rigid body motion of the blade in the straps. All rigid body modes occur under 2.7 Hz with the rigid body bounce mode occurring at 2.0 Hz for the single strap test with the first flexible mode inline with the bungees at

about 25 Hz. This provided greater than the normally accepted factor of 10 in frequency separation from the suspension dynamics [2]. If inadequate frequency separation between the suspension and blade modes were to occur, it would be possible to reduce the stiffness of the coiled bungee rope by reducing the number of turns of the rope used to support the blade. This was not necessary for these tests.

Figure 2. Double Strap Suspension Configuration

Figure 3. Single Strap Suspension Configuration

There are several constraints we consider regarding the suspension procedure. Firstly, no load could be applied to the trailing edge of the blade. The trailing edge is fragile and is aerodynamically critical for optimum performance. By suspending the blade leading edge down, the trailing edge would see no concentrated load. Secondly, the bungee cords are a weak point in the suspension system. Precautions were taken to limit the time for which the blade was suspended since elongation of the bungee cords over time could limit control of the blade. Therefore, as a precaution the storage cradles remained positioned underneath the blade during testing and the blade was only lifted enough to completely free it from the cradles. The blade was promptly returned to the storage cradles when testing was completed.

The instrumentation of an individual blade consisted of 68 accelerometers rated to 50 g's. The accelerometers were carefully placed on the blade so as not to damage the blade's finish. All of the mounting locations utilized a biaxial setup as seen in Figure 4. Accelerations were measured in both the x- and z-direction while acceleration in the y-direction (axial direction) was neglected. See Figure 3 for a triad defining these reference directions. The final instrumentation consisted of two perpendicular accelerometers positioned at all 34 mounting locations. The total mass of the accelerometers, mounting blocks, and cables was close to 3 pounds. The nominal blade mass is 361 pounds. We refer to this set of 34 locations (68 accelerometers) as the fully instrumented set. In order to evaluate mass loading effects, we also re-tested with a lightly instrumented set of only 4 accelerometers. All the accelerometers were oriented with no more than 3 degree error for all three axes as determined by a digital inclinometer. Any orientation error can be attributed to uneven settling of the dental cement used to secure the blocks as well as measurement error. A description of the procedure for mounting the accelerometers is thoroughly documented in Appendix C. A list of the coordinates for the accelerometer locations is given in Appendix D.

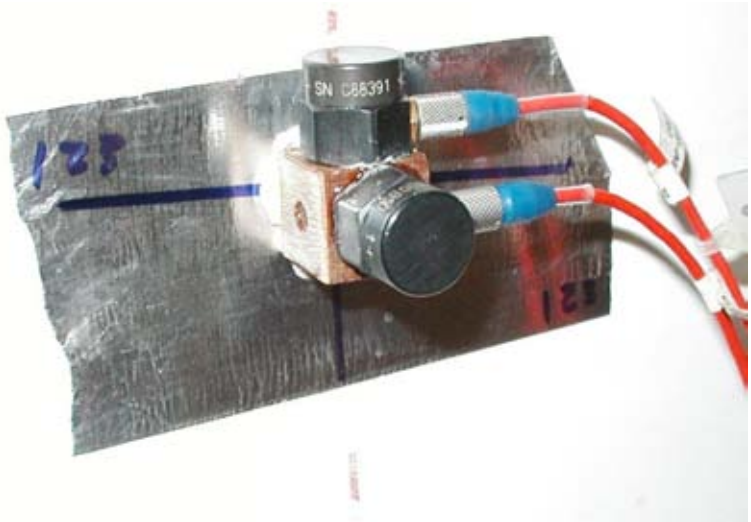

Figure 4. Biaxial Accelerometer Mounting

Nine data sets were acquired for each blade corresponding to nine different force excitation location/direction pairs. The structure was excited using a 3 lb impact hammer. Six excitation locations were in the x-direction while the remaining three were in the z-direction. In this way, we expect that both flapwise and edgewise bending modes are excited. Flapwise bending refers to bending about the z-axis while edgewise bending refers to bending about the x-axis (See Figure 3 for

definition of directions). Excitation in the x-direction was performed at points low and high on the blade (i.e. near the leading edge and near the trailing edge) and near and distant from the root end and suspension in an attempt to better excite all the modes of the structure, particularly the coupled bending and torsional modes.

These tests were conducted at the FAA Airworthiness Assurance NDI Validation Center in Albuquerque, NM. The tests were conducted in a large aircraft hangar in an uncontrolled temperature environment. The temperature increase can be as much as 15 degrees over the course of a typical work day from morning to afternoon. For each test, temperature was recorded. The temperature variation for a particular test was 8 degrees Fahrenheit or less.

For these tests, data was acquired using a 16 second window. Although difficult to achieve, this provided a better data sample than shorter samples. However, there are some issues that make a long acquisition window difficult for these tests. The test location is adjacent to the Albuquerque Sunport, which experiences frequent commercial and military traffic. In addition, many smaller aircraft stage for flight within 500 yards of the hangar. Data cannot be recorded while these events are taking place, and many times data sets had to be rejected when these unexpected events occur. Often it is difficult to find an acceptable 16 second window for acquisition. In the interest of protecting the blades, the blades were lifted minimally from the cradles. It is possible for the blades to rigidly rotate during a test potentially causing contact with the storage cradles and disturbing the results. The possibility of this occurring is accentuated with a longer acquisition window.

Data Analysis

The modes for each test were extracted from each data set using the Synthesis Modes and Correlate (SMAC) algorithm developed at SNL [3,4]. The SMAC algorithm is based upon modal filtering, and was designed to extract modal parameters from frequency response functions (FRFs). The SMAC algorithm is highly automated – over 90% of the modes of interest are identified automatically. Any remaining modes (frequency and damping) which are not identified automatically must be fit manually. Basically, a frequency and damping range is chosen, and an improved guess for frequency and damping can be found by maximizing the correlation between the experimental data and the SMAC single degree of freedom second order curve fit. When converged, the new mode is added to the mode set. The final product is a synthesis of the FRFs using the analytically fit modes. This synthesized FRF is compared to the test FRF.

The analytically fit modes of each impact test were then compared using the MultiSort algorithm that was also developed at SNL [5]. This program is used to compare modal parameters from multiple modal tests. For this work, we compared the modal parameters identified from each of the tests performed at different locations/directions of force input in an effort to extract the most satisfactory modes. This algorithm provides insight through numerical metrics in choosing the most accurate mode.

The modal assurance criterion (MAC) algorithm was utilized to evaluate the correlation, in a vector sense, between two sets of modes. Essentially, MAC provides a matrix of correlation values for the identified mode shape vectors. When the MAC is diagonally dominant with small off-diagonal entries, the modes are linearly independent. A standard practice is to compute the MAC for the experimental

modes with themselves in order to justify the choice of sensor locations. Such a correlation shows the linear independence of the modes and gives an indication of the completeness of the set of accelerometer locations chosen for fully capturing the structural dynamics. The absence of high correlations in off-diagonal entries as seen in Figures 5 and 6 indicates that both the amount and location of accelerometers are appropriate for this test, for Blade #001 and #003 respectively. Of course, the diagonal values are 100% correlated since we have computed the MAC of itself in each case.

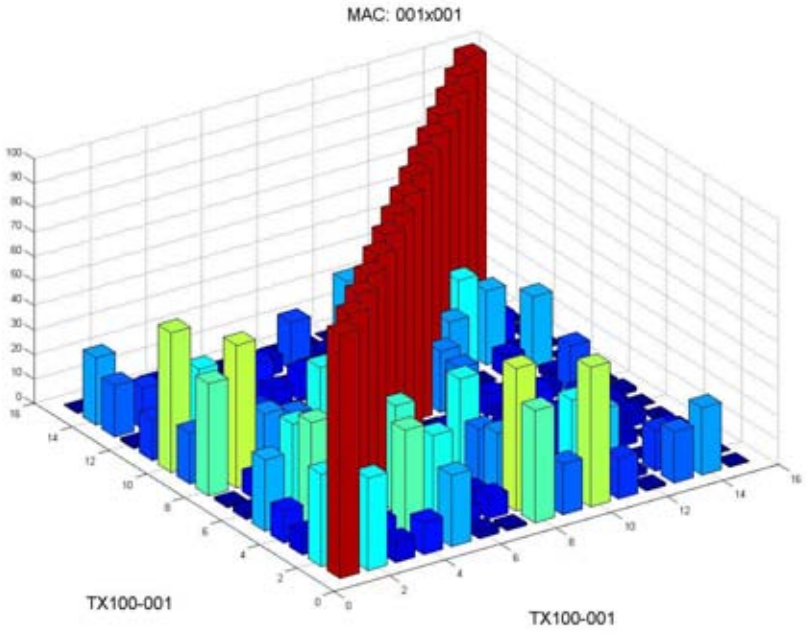

Figure 5. MAC Plot for Blade #001 to Blade #001

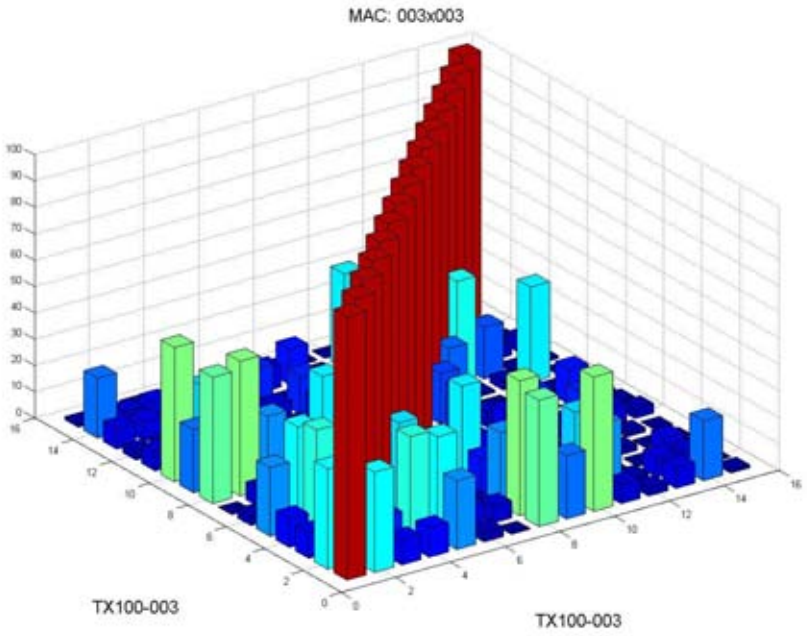

Figure 6. MAC Plot for Blade #003 to Blade #003

The MAC algorithm is also used to identify the modes that are common to both blades. Here we are looking at the correlation between the data sets which result from using the Multisort algorithm. We are also interested in evaluating unit to unit variability between the two blades, and MAC allows us to find the common modes for comparison of modal parameters. The MAC for the mode shapes of Blade #001 and Blade #003 is shown in Figure 7. The high correlation coefficient among the diagonal entries indicates that the two blades share these modes. The small off-diagonal entries indicate that those modes are not highly correlated whereas larger off-diagonal correlation in Figure 7 (and Figures 5 and 6 as well) indicates more correlation in those modes. The actual values for the diagonal entries of Figure 7 are plotted in Figure 8. The higher the correlation, the more confidence there is that the same mode is present in both data sets. Of course, the lower order modes are more easily identified; however, all modes reported have "confidence" of greater than 84%, and are clearly identified by their mode shape.

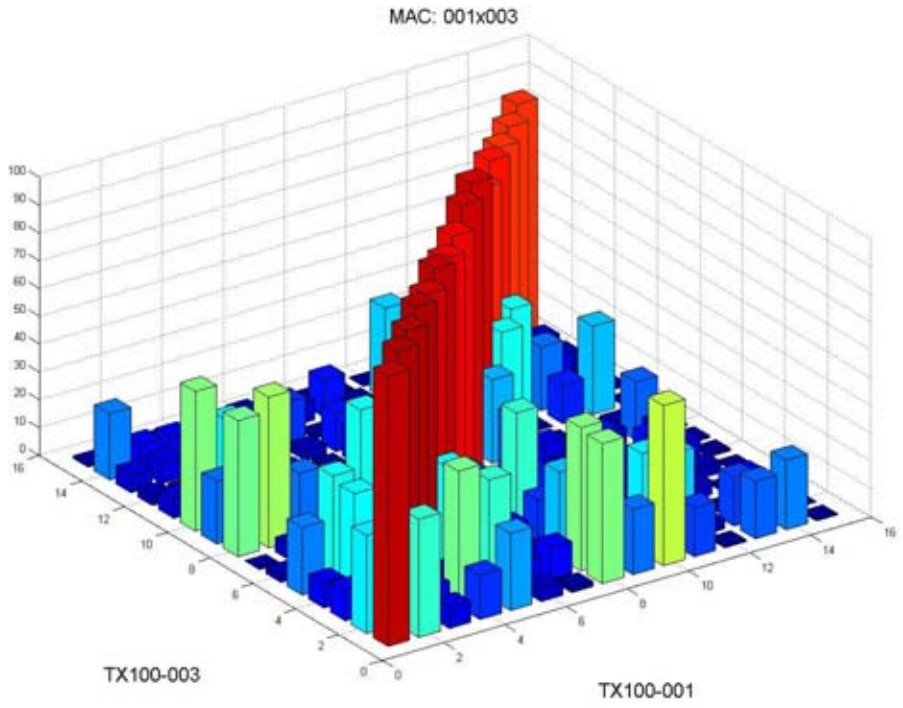

Figure 7. MAC Plot for Blade #001 to Blade #003

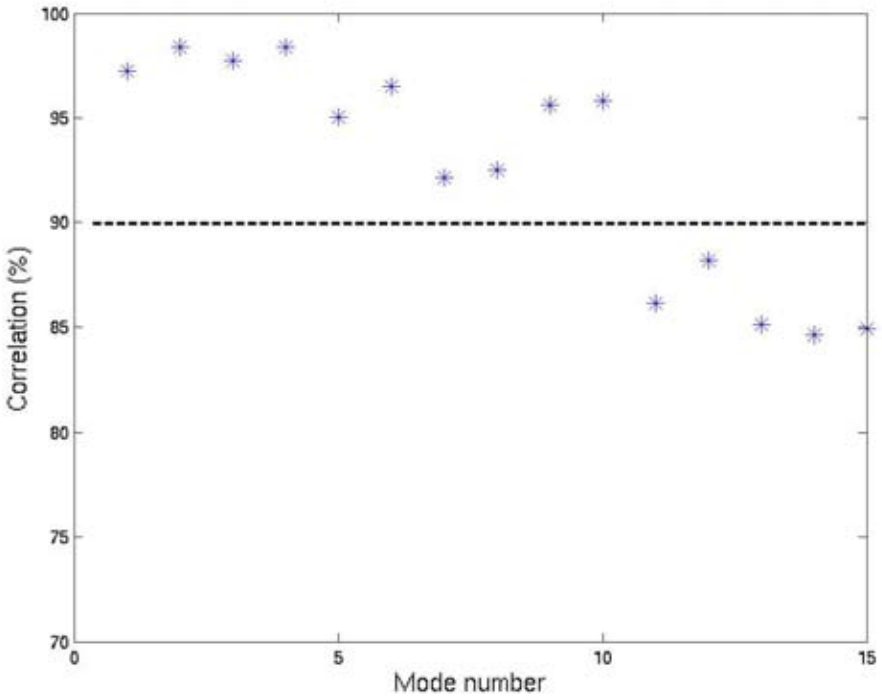

Figure 8. Plot of MAC Diagonal Values for Blade #001 to #003

Modal Survey Results

The results for the natural frequencies and damping are given in Table 1. The description of each mode is determined by viewing the experimental mode shapes and by comparing them with the theoretical mode shapes for a free-free beam [6]. The fifteen modes listed in Table 1 represent the best modes of these data sets for the purpose of validating numerical finite element models, and are tabulated from lightly instrumented tests with single strap suspension. It was found that the natural frequencies extracted from the fully instrumented data set were consistently several tenths of a hertz less than those from the lightly instrumented data sets. The analysis of the data revealed that the tests with impacts along the 130 nodal line (See Figure D-1 in Appendix D) provide a sufficient sample; therefore only the data sets for the lightly instrumented with impacts at 131x (location 131 in the x-direction), 133x, and 131z were processed. Included in the modal survey results are eleven modes which can be categorized by mode shape including the first five flapwise bending modes, the first three edgewise bending modes, and the first three torsional modes. Flapwise bending refers to bending about the z-axis while edgewise bending refers to bending about the x-axis. Four additional modes are included which have been labeled "Coupled mode". These are strong modes which are difficult to categorize by mode shape, but may be useful for validation purposes. The modes associated with the suspension include a bounce mode in which the blade translates rigidly in the z-direction at 2 Hz (for the one strap test, and 4 Hz for the two strap test), and a roll/pendulum mode in which the blade rolls/swings rigidly in the straps at 2.7 Hz.

Table 1. Frequency and Damping List for Individual Modes

Mode Number	Mode Description	Blade TX 100-001		Blade TX 100-003	
		Frequency (Hz)	Damping (%)	Frequency (Hz)	Damping (%)
1	1st flapwise	6.44	0.27	6.49	0.20
2	2nd flapwise	15.16	0.26	15.14	0.23
3	1st edgewise plus 2nd flapwise	25.00	0.32	25.25	0.34
4	3rd flapwise plus 1st edgewise	28.44	0.31	28.94	0.60
5	4th flapwise plus some 2nd edgewise	43.89	0.37	43.92	0.34
6	2nd edgewise plus some 4th flapwise	54.55	0.41	55.31	0.39
7	1st torsion plus some 2nd edgewise	58.00	0.71	58.82	0.48
8	5th flapwise plus some 2nd edgewise	63.69	0.49	64.20	0.31
9	Coupled mode #1	75.13	0.56	76.39	0.58
10	Coupled mode #2	82.13	0.50	83.92	0.64
11	Coupled mode #3	85.59	0.52	86.13	0.51
12	2nd torsion and 2nd edgewise	88.53	0.80	87.94	0.56
13	Coupled mode #4	95.06	0.66	96.81	0.58
14	3rd edgewise	101.04	0.57	102.75	0.47
15	3rd torsion	107.13	0.73	107.81	0.90

These results indicate that Blade #003 is slightly stiffer than Blade #001 with generally higher natural frequencies. A numerical comparison of each mode in Table 1 is given in Table 2 showing the percent difference in the natural frequency and damping. In a relative sense, no mode varies by more than 2.2 % in frequency. The larger variations typically occur with the highly coupled modes. The lower order modes are very similar in frequency and damping in an absolute sense. Damping values, on the other hand, do not show such a strong trend when comparing the two blades.

The mode shapes of Blade #001 and #003 are available in Appendices A and B, respectively.

Table 2. Blade Comparison

Mode Number	Mode Description	Percent Difference (#003 minus #001)/#001	
		Frequency	Damping
1	1st flapwise	0.7	-23.0
2	2nd flapwise	-0.1	-11.2
3	1st edgewise plus 2nd flapwise	1.0	6.2
4	3rd flapwise plus 1st edgewise	1.8	93.0
5	4th flapwise plus some 2nd edgewise	0.1	-6.5
6	2nd edgewise plus some 4th flapwise	1.4	-3.9
7	1st torsion plus some 2nd edgewise	1.4	-31.8
8	5th flapwise plus some 2nd edgewise	0.8	-36.3
9	Coupled mode #1	1.7	3.7
10	Coupled mode #2	2.2	28.0
11	Coupled mode #3	0.6	-3.3
12	2nd torsion and 2nd edgewise	-0.7	-29.7
13	Coupled mode #4	1.8	-11.0
14	3rd edgewise	1.7	-18.5
15	3rd torsion	0.6	24.1

Further Experimental Considerations

The testing procedure and site presented several uncontrollable variables, including ambient temperature, suspension setup, and mass-loading of the blade due to instrumentation. In an effort to investigate these effects, separate tests were conducted to measure the effect, if any, which these variables have on the test results.

The plot in Figure 9 is an overlay of two FRFs (frequency response functions), one represents a fully instrumented blade (red) and the other represents a lightly instrumented blade (blue), for the same blade and excitation location. A fully instrumented blade is instrumented with 68 accelerometers and a lightly

instrumented blade has only four accelerometers – two each at locations 131 and 133. Both FRFs in Figure 9 are from Blade #001 and represent a driving point FRF for location 131x. For the fully instrumented blade, the FRF is slightly shifted to a lower frequency, which is most likely the result of the added mass or mass-loading effect of the instrumentation. For this reason, the natural frequencies and damping reported in Table 1 are computed from the lightly instrumented data sets although the effect is small. Mode shapes, of course, must be identified from the fully instrumented data sets which provide the spatial resolution needed to identify the modes.

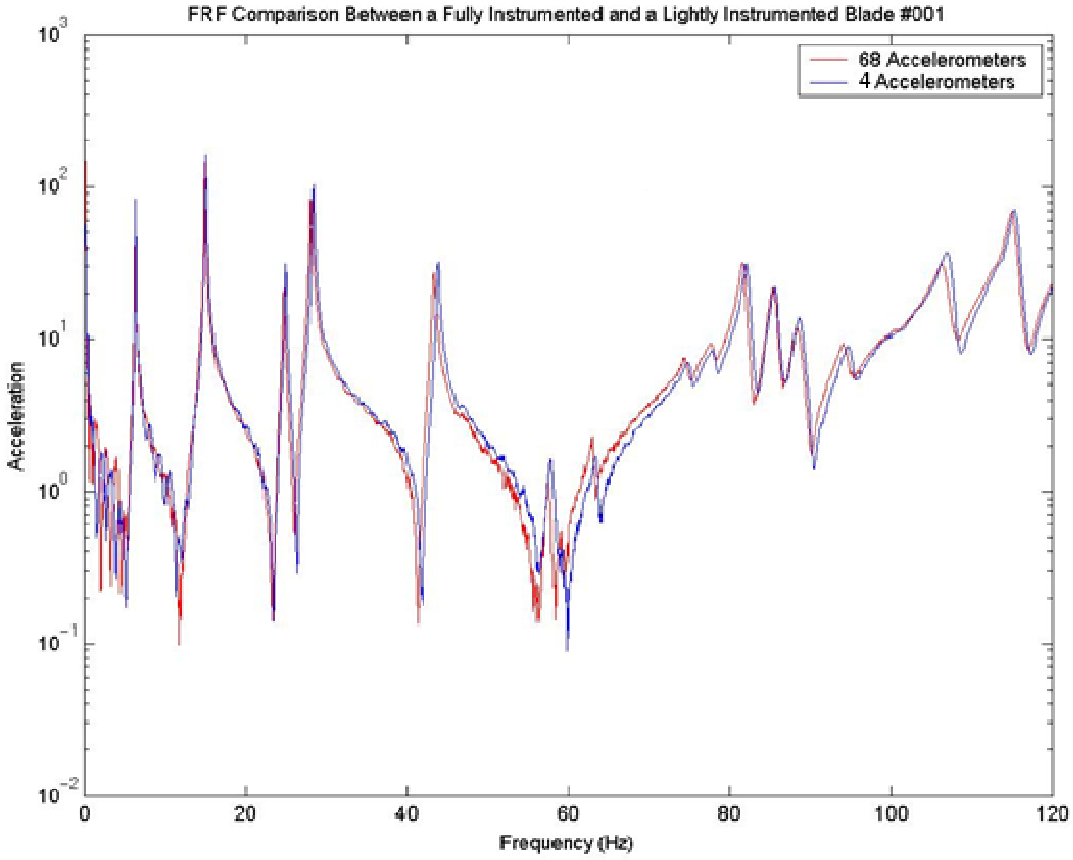

Figure 9. FRF Comparison of Fully and Lightly Instrumented Blade

We can perform some calculations to estimate the mass loading effect. Consider Eq. (1) which gives the ratio of measured natural frequency (ω_m) for an instrumented blade to the true natural frequency (ω_t). We assume a simple single degree of freedom model with no change in stiffness.

$$\frac{\omega_m}{\omega_t} = \sqrt{\frac{k/m_m}{k/m_t}} = \sqrt{\frac{m_t}{m_m}} = \sqrt{\frac{m_t}{m_t + \Delta m}} \tag{1}$$

For a 361 pound blade with 3 pounds of sensor mass loading, we estimate a frequency change due to mass loading of 0.4%.

The plot shown in Figure 10 is an overlay of two FRFs, one represents a lightly instrumented Blade #001 (red) and the other represents a lightly instrumented Blade #003 (blue). The blades were tested in as close to identical environments as possible on consecutive days. Both FRFs are driving point FRFs at location 131x. Figure 10 indicates that blades are quite similar at low frequency; however, the FRF of Blade #001 is shifted to lower frequency above 45 Hz.

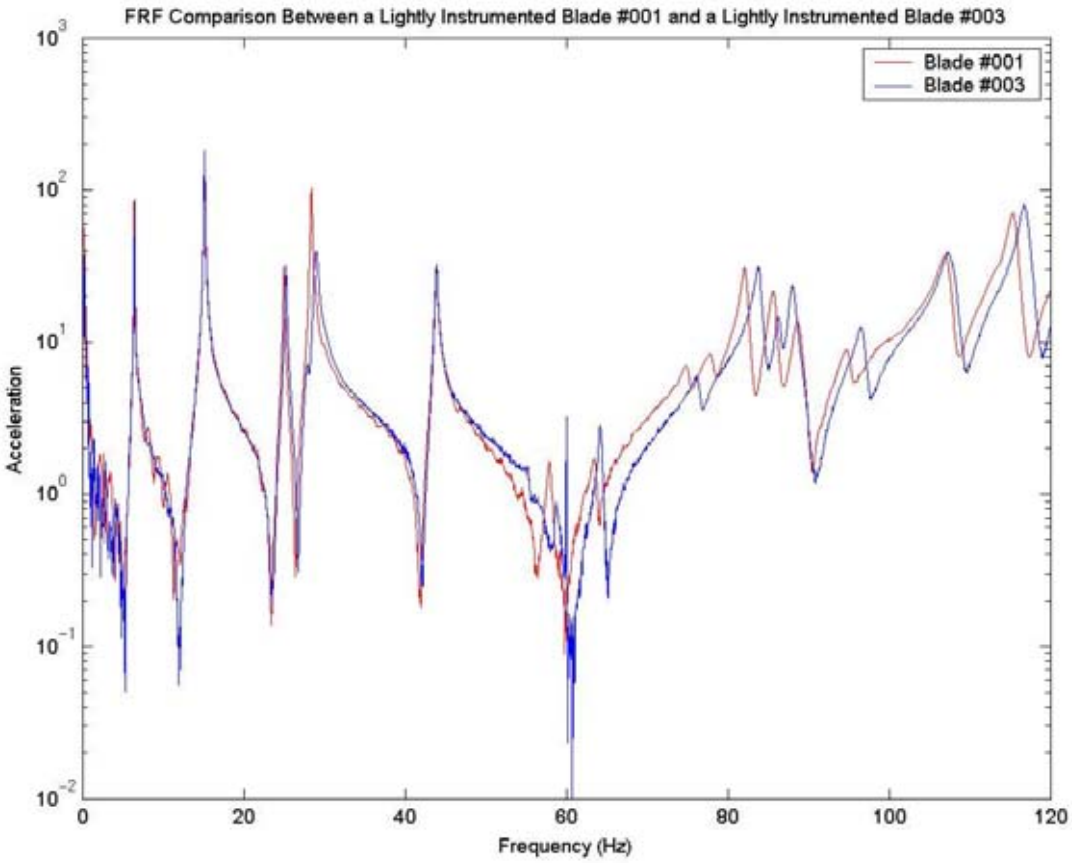

Figure 10. FRF Comparison of Lightly Instrumented Blades #001 and #003

The plot in Figure 11 is an overlay of two FRFs, one represents a double strap suspension (red) and the other represents a single strap suspension (blue). Both FRFs are from Blade #003 and represent driving point FRFs at location 163x. The FRFs are very similar throughout the frequency range except the slightly increased damping of the double strap response.

The effect of the choice of the number of supporting straps is less significant than the variability from one blade to another as seen in Figure 10. Increased damping in the double strap suspension was found for these tests whereas differences in frequency were quite small. Additionally, the bungee mode of the suspension occurs at about 4 Hz for the double strap setup as opposed to 2 Hz for the single strap setup. Thus with two straps, the frequency separation of the suspension and elastic modes of the structure is reduced. Although a double strap suspension setup offers more control over the blade and permits less rotation due to impact, the one strap setup offers sufficient blade control without the need for an additional second tripod. Additionally, less added damping and better frequency separation from the suspension modes are found for the one strap suspension approach. Thus the one strap suspension is preferred for several reasons, but should only be used as long as proper safety margins are in place for blade control during testing.

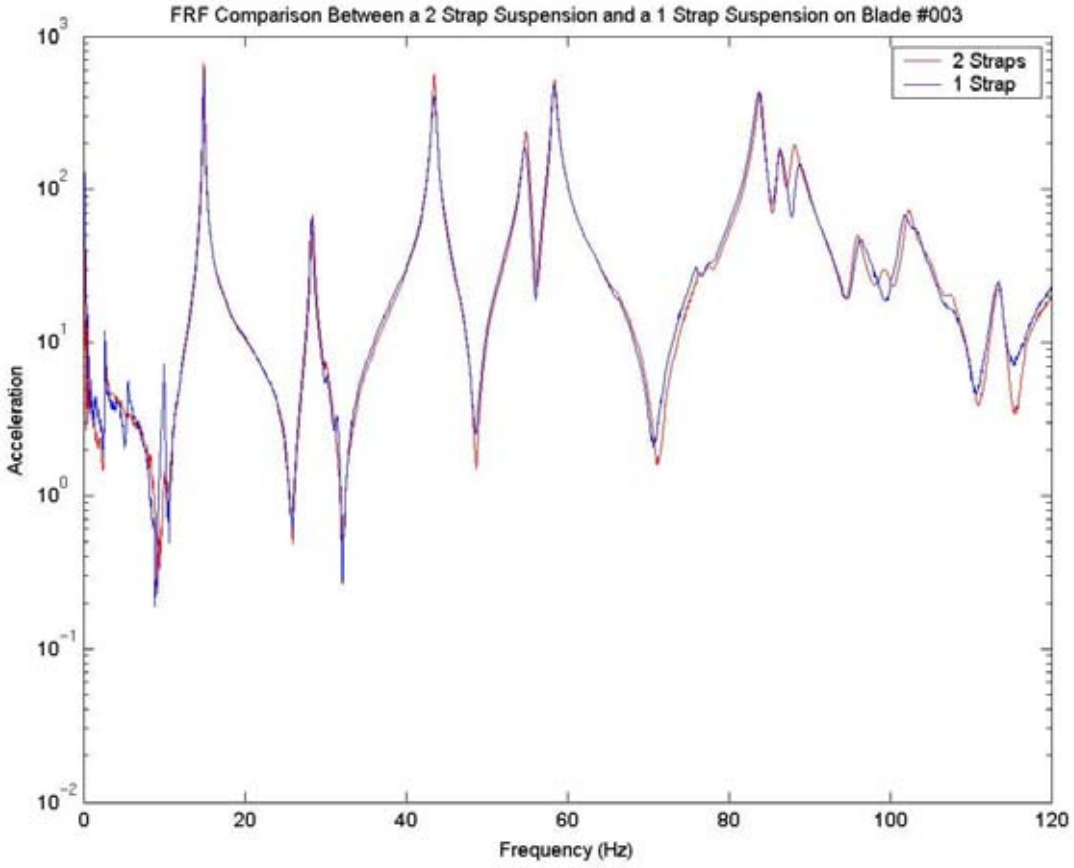

Figure 11. FRF Comparison of Single and Double Strap Suspension

Quantification of Uncertainty in Modal Parameters

In Reference 7, the test to test variability of the modal parameters was quantified for the first eight modes listed in Table 1 for the TX-100 blades. No additional testing was performed for the sole purpose of evaluating the variation of the modal parameters from test to test, that is, the test to test variability. One could repeat a test several times with all controllable variables constant to see how the modal parameters vary; however, no time was spent on this task for these tests. Therefore, we took a different approach to evaluating test to test variability by assessing the individual effects on test to test variability due to force input location as well the effect of environmental factors such as mass loading, support conditions, temperature were considered. A limited number of comparable test data sets were available for this analysis which is a limitation to more rigorous uncertainty quantification. This situation is common in practice, yet some analysis can still be performed. Modal parameter estimation algorithms typically are very accurate for frequency estimates yet are not quite as accurate for the damping estimates. Therefore, we attempted no quantification of uncertainty on the damping values because of the uncertainty in their estimation. We focus only on the test to test variability in the frequencies in this report.

In summary, we consider quantifying the total uncertainty in the frequencies due to environmental and force input location variability. Without rigorous uncertainty estimation, we look to worst case uncertainty of each source considered to be a random error and consider the following measure of test to test uncertainty [8]:

$$U_{test} = \sqrt{U_{mass}^2 + U_{spcond}^2 + U_{temp}^2 + U_{force}^2} \tag{2}$$

where the first three terms on the right hand side represent the environmental uncertainty, and the final term represents the force input location uncertainty. We apply this metric to the worst case values determined from the test data in Table 3, with the test to test or total uncertainty given on the next to the last line of the table with a value of 2.1%.

Table 3. Test to Test Variability for Natural Frequency

Uncertainty Parameter	TX-100 Uncertainty (%)
U-mass loading	1.9
U-support conditions	0.6
U-temperature	0.4 (assumed)
U-input location	0.6
U-test to test (worst case)	***2.1%***
U-test to test	***0.7%***

The largest unit to unit variability is found to be 1.8% and the smallest at 0.1% from Table 2. This shows that the test to test variability, computed as conservatively as possible using the worst case scenario in which mass loading and support conditions are considered as random error, is slightly larger

than the unit to unit variations. Thus, we cannot determine if the trends in the unit variations are valid by this method.

On the other hand, we can consider the mass loading and support conditions as bias error or simply a shift in the data and ignore them in Eq. (2). In this case we find the largest value for the test to test variability to be 0.7% for the first and sixth modes, with values ranging from 0.4% to 0.7% for the first eight modes. In this case, the unit variations are still difficult to validate although the unit variations trend strongly and the majority of the unit variations are larger than the test to test variations observed on a mode by mode basis. Considering only the test to test variations due to temperature and force input location is the more appropriate because mass loading and support conditions are nominally constant for a test and were the same for each of the blades tested in this study.

Conclusion

The results detailed in this report provide enough information to judge the validity of a finite-element model for the TX-100 series wind turbine blades. Two nominally identical blades were tested. The frequency, damping and mode shapes provided have been analyzed to determine their accuracy, and the uncertainty due to environmental factors and force input location was quantified. It can be seen that the construction method results in some variation from blade to blade, although the blades are quite similar. These results establish a small range of values for natural frequency and damping for these blades to be used for model validation. Several factors, which may have affected the accuracy of these results have been evaluated and consequently play little or no role in the resulting accuracy of this experimental modal survey. It was determined that the single strap suspension configuration in which the blade is supported at only one point, the center of gravity, has some advantages in minimizing the effect of support conditions although more blade control is found for the double strap method. Forcing input along a nodal line near the mass center of the blade is a preferred excitation location. Forcing at this location tends to excite the torsional modes and coupled bending and torsional modes, as well as other modes of interest.

References

[1] Joosse et al., "Cost Effective Large Blade Components By Using Carbon Fibres," *Proc. of the 2002 ASME Wind Energy Symposium Technical Papers*, 40th AIAA Aerospace Sciences Meeting and Exhibit. Reno, Nevada. January 14-17, 2002, 47-55.

[2] Carne, Thomas G., and Dohrmann, Clark R., "Support Conditions, Their Effect on Measured Modal Parameters," *Proceedings of the 16th International Modal Analysis Conference*, pp. 477-483, February 1998.

[3] Mayes, Randall L. and Klenke, Scott E., "The SMAC Modal Parameter Extraction Package," *Proceedings of the 17th International Modal Analysis Conference*, pp. 812-818, February 1999.

[4] Mayes, Randall L. and Klenke, Scott E., "Automation and Other Extensions of the SMAC Modal Parameter Extraction Package," *Proceedings of the 18th International Modal Analysis Conference*, pp. 779-785, February 2000.

[5] Mayes, Randall L. and Klenke, Scott E., "Consolidation of Modal Parameters from Several Extraction Sets," *Proceedings of the 19th International Modal Analysis Conference*, pp. 1023-1028, February 2001.

[6] Blevins, Robert D., *Formulas for Natural Frequency and Mode Shape*, Kreiger, Malabar, Florida, 1995.

[7] Griffith, D. Todd, Casias, Miguel, Smith, Gregory, Paquette, Josh, and Simmermacher, Todd, "Experimental Uncertainty Quantification of a Class of Wind Turbine Blades," *24th International Modal Analysis Conference*, February 2006, SAND2005-6624C.

[8] Coleman, Hugh W., and Steele, W. Glenn, *Experimentation and Uncertainty Analysis for Engineers*, WileyInter-Science, New York, 1999.

Appendix A
Mode Shapes of Blade Serial #TX-100-001

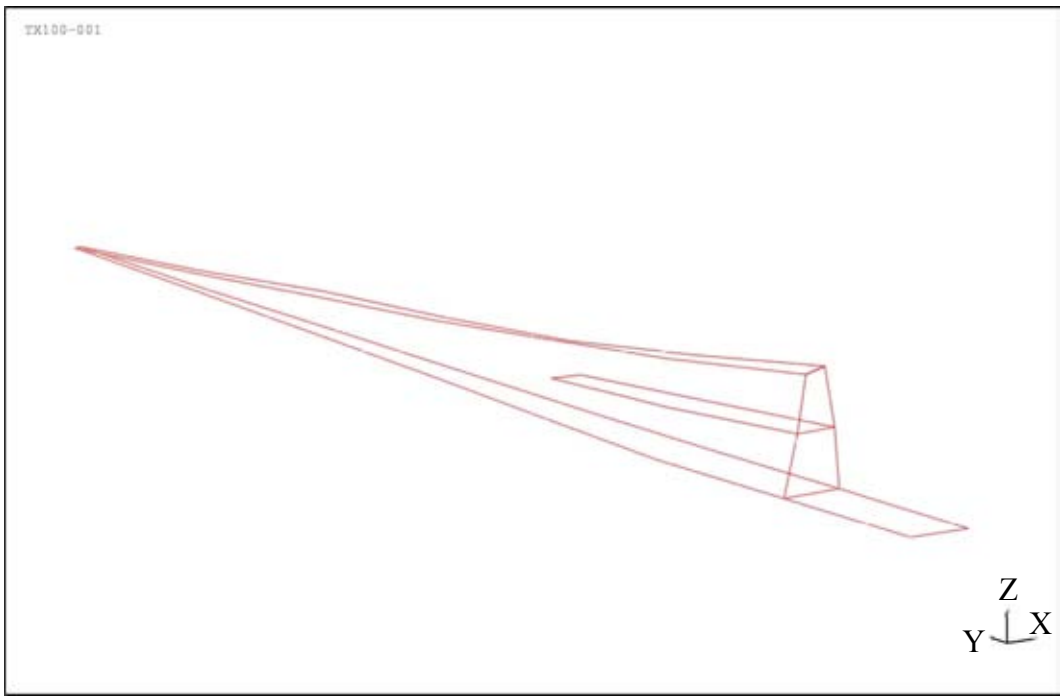

Figure A-0. Undeformed Blade Serial #TX-100-001

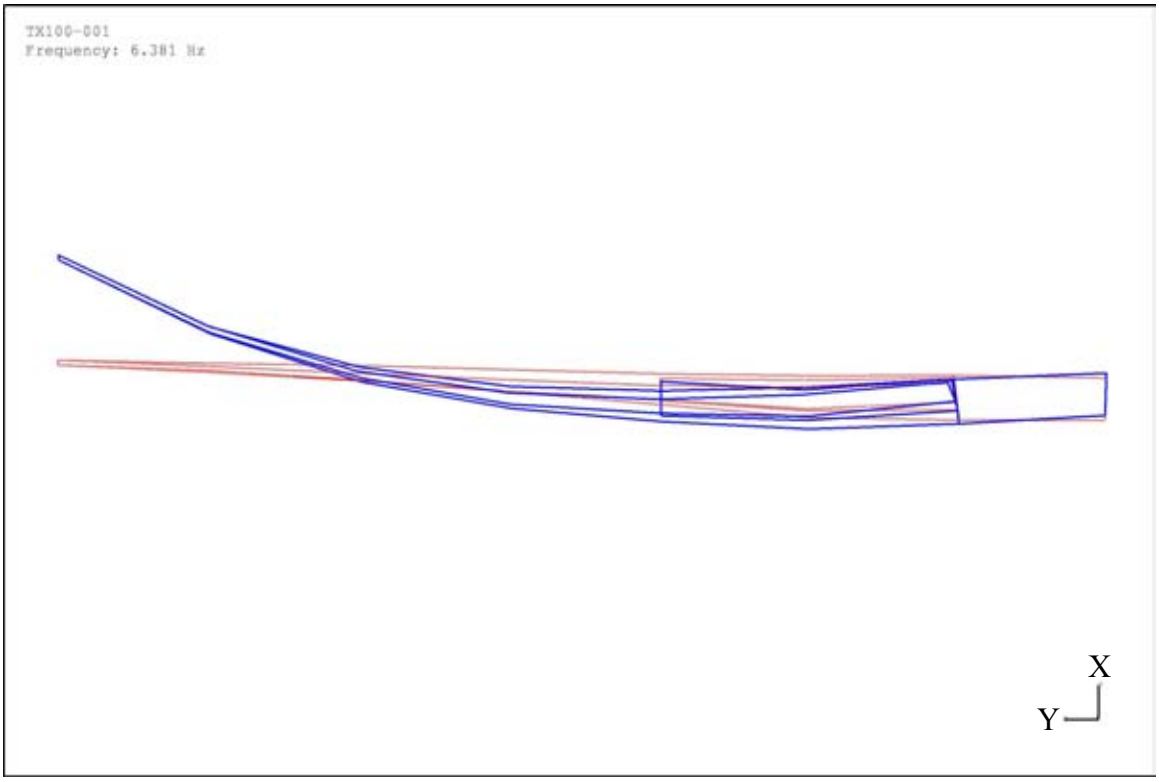

Figure A-1. First Flapwise Mode (f = 6.44 Hz, ζ = 0.27 %) Blade Serial #TX-100-001

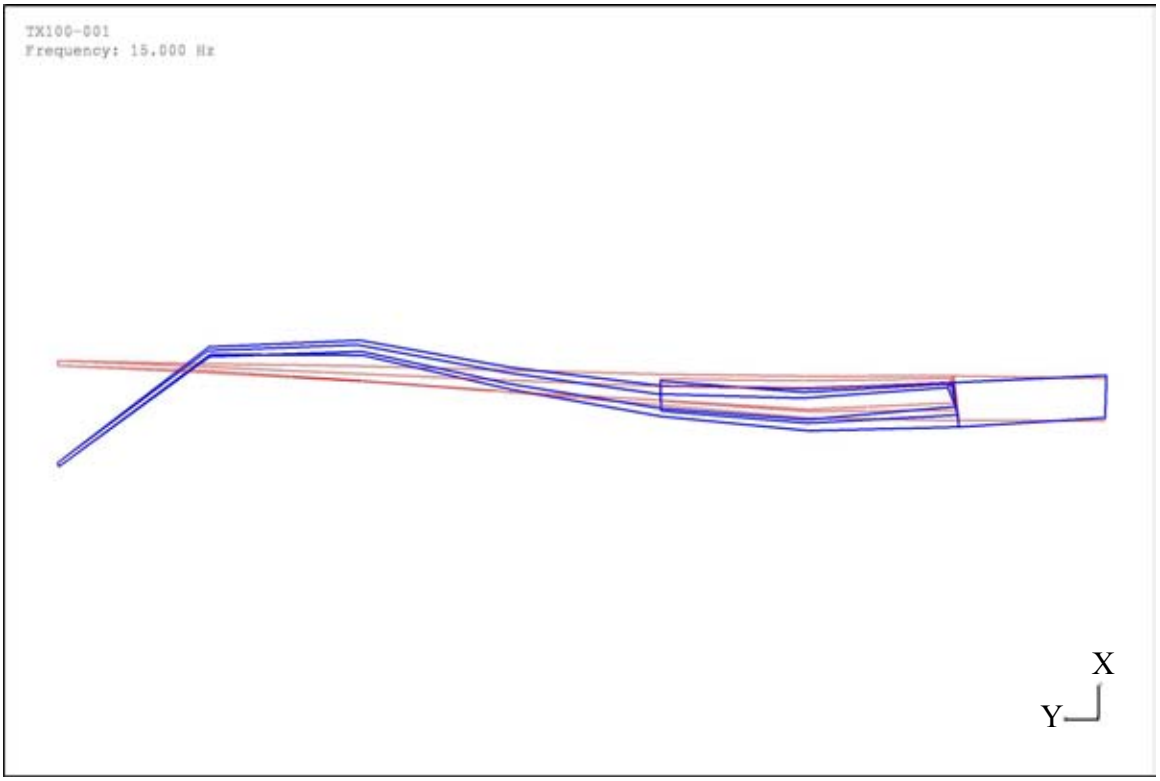

Figure A-2. Second Flapwise Mode (f = 15.16 Hz, ζ = 0.26 %) Blade Serial #TX-100-001

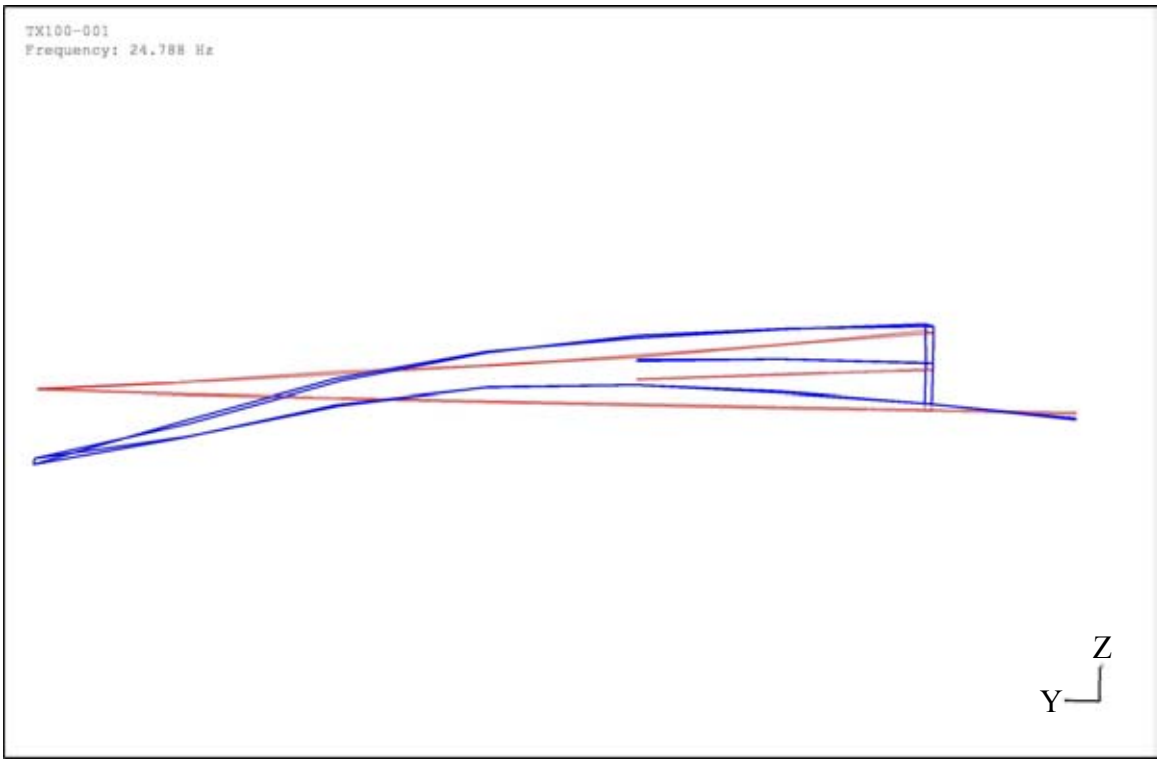

Figure A-3. First Edgewise Mode (f = 25.00 Hz, ζ = 0.32 %) Blade Serial #TX-100-001

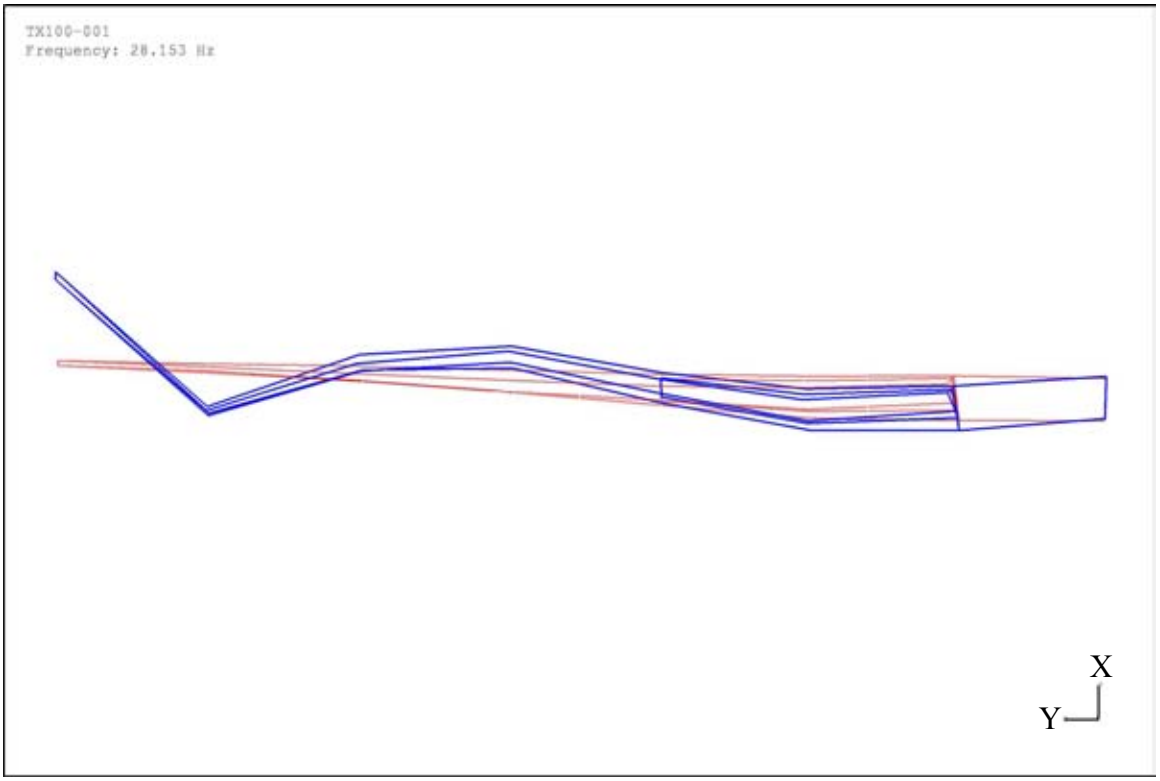

Figure A-4. Third Flapwise Mode (f =28.44 Hz, ζ = 0.31 %) Blade Serial #TX-100-001

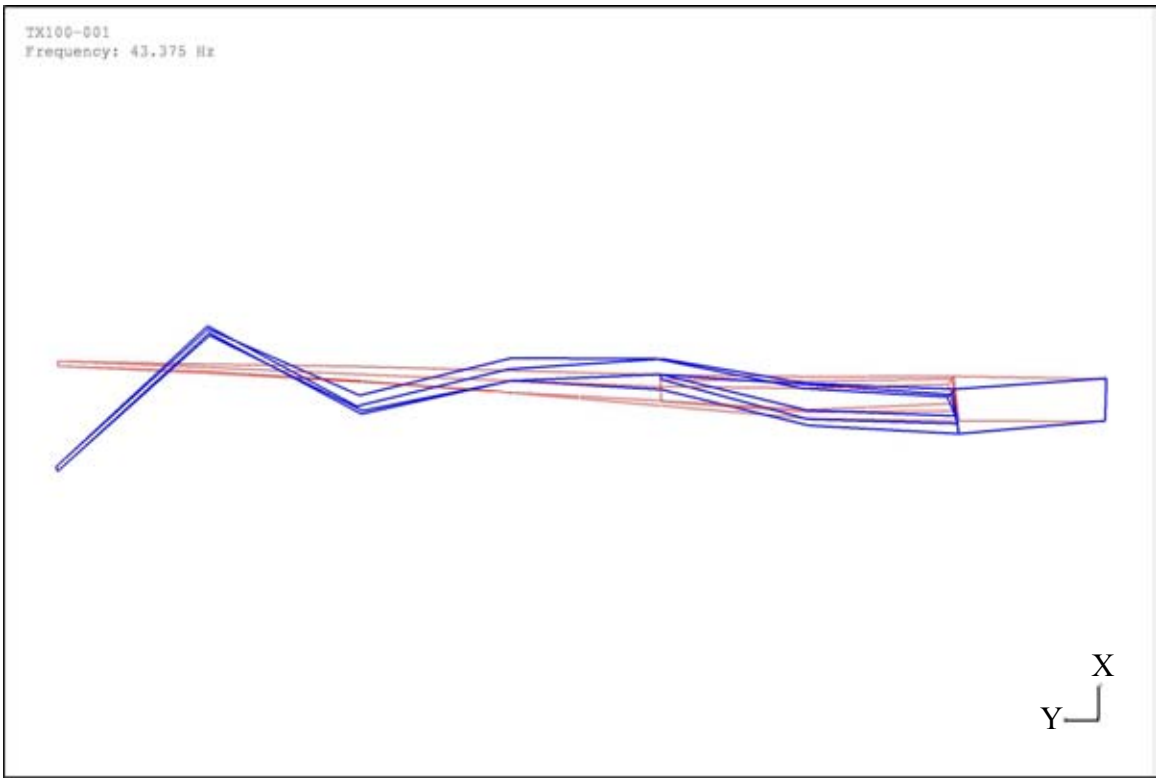

Figure A-5. Fourth Flapwise Mode (f = 43.89 Hz, ζ = 0.37 %) Blade Serial #TX-100-001

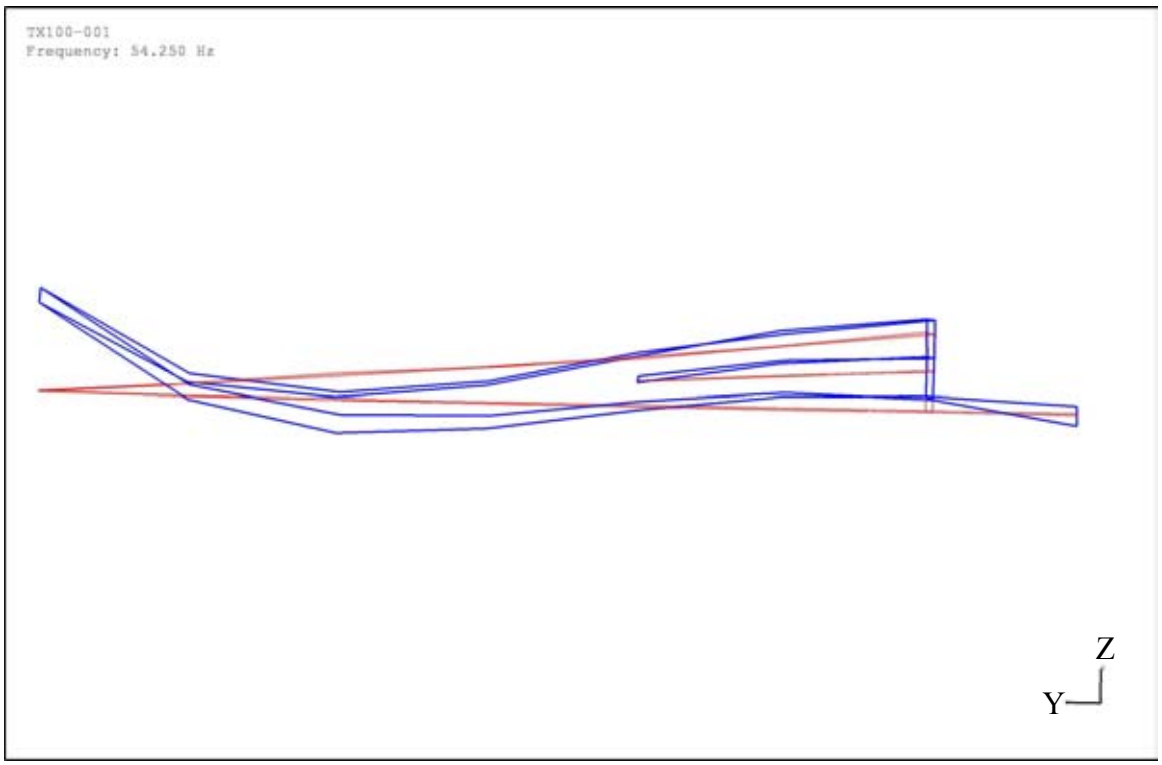

Figure A-6. Second Edgewise Mode (f = 54.55 Hz, ζ = 0.41 %) Blade Serial #TX-100-001

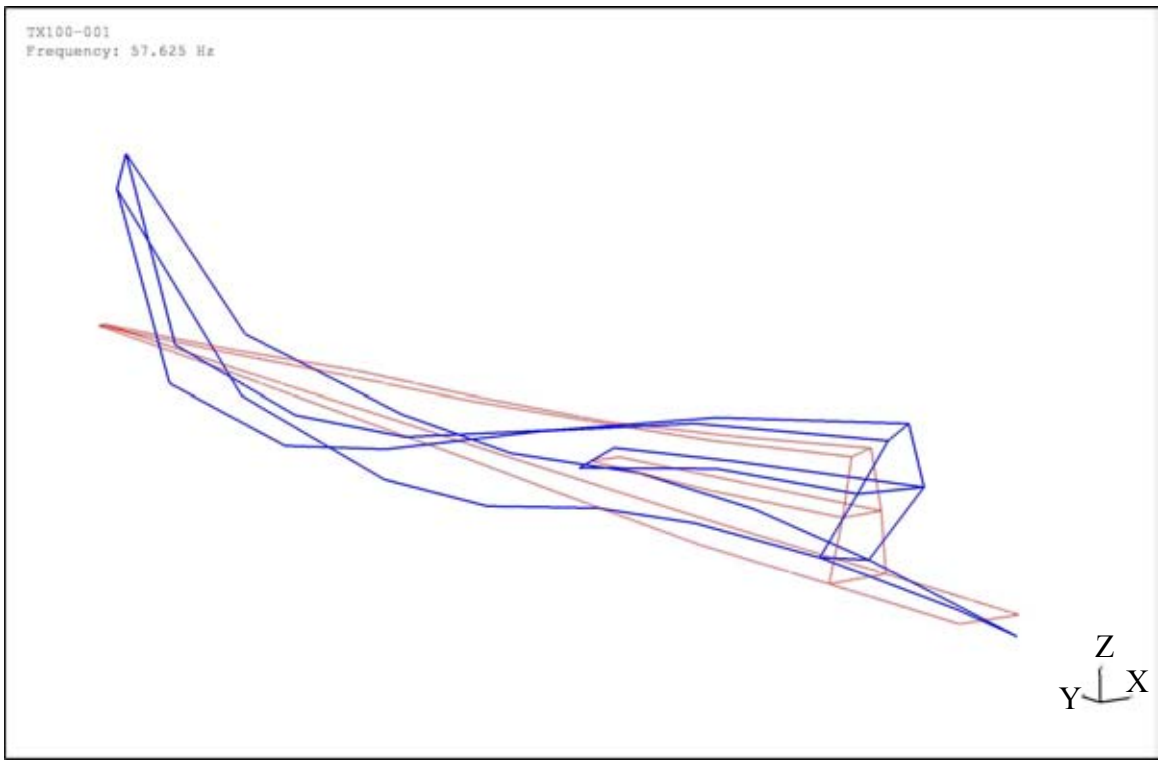

Figure A-7. First Torsional Mode (f = 58.00 Hz, ζ = 0.71 %) Blade Serial #TX-100-001

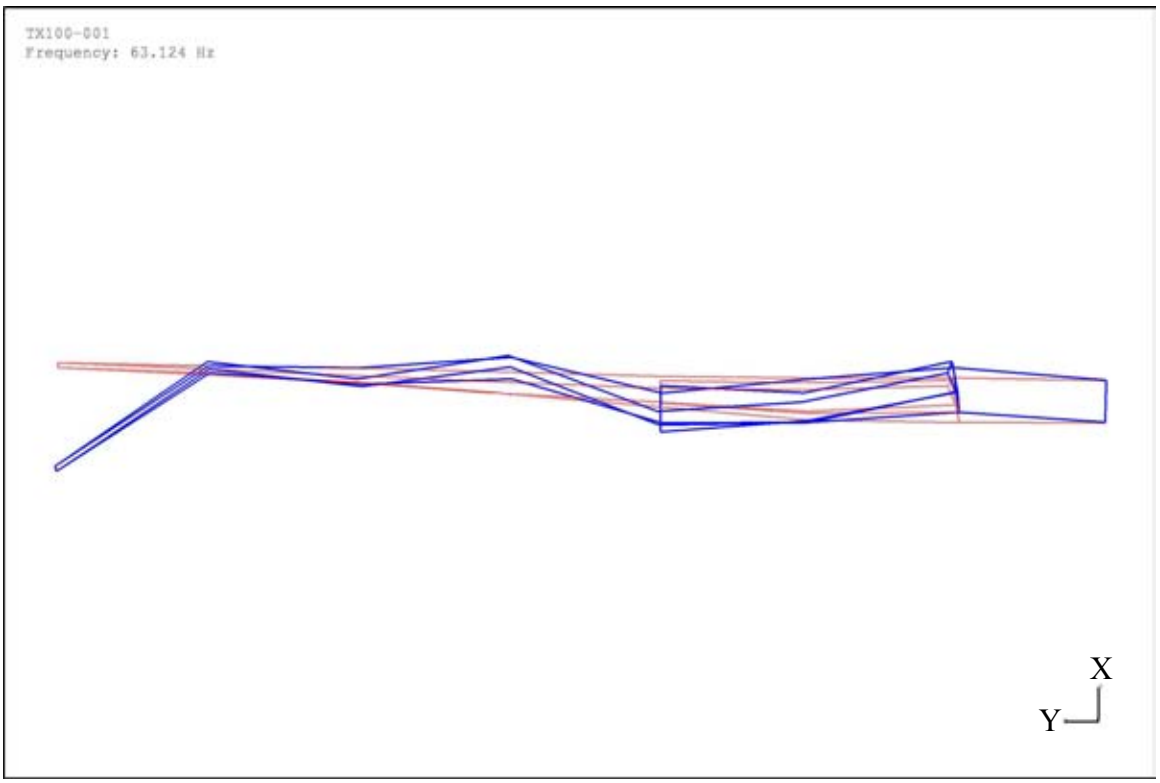

Figure A-8. Fifth Flapwise Mode (f =63.69 Hz, ζ = 0.49 %) Blade Serial #TX-100-001

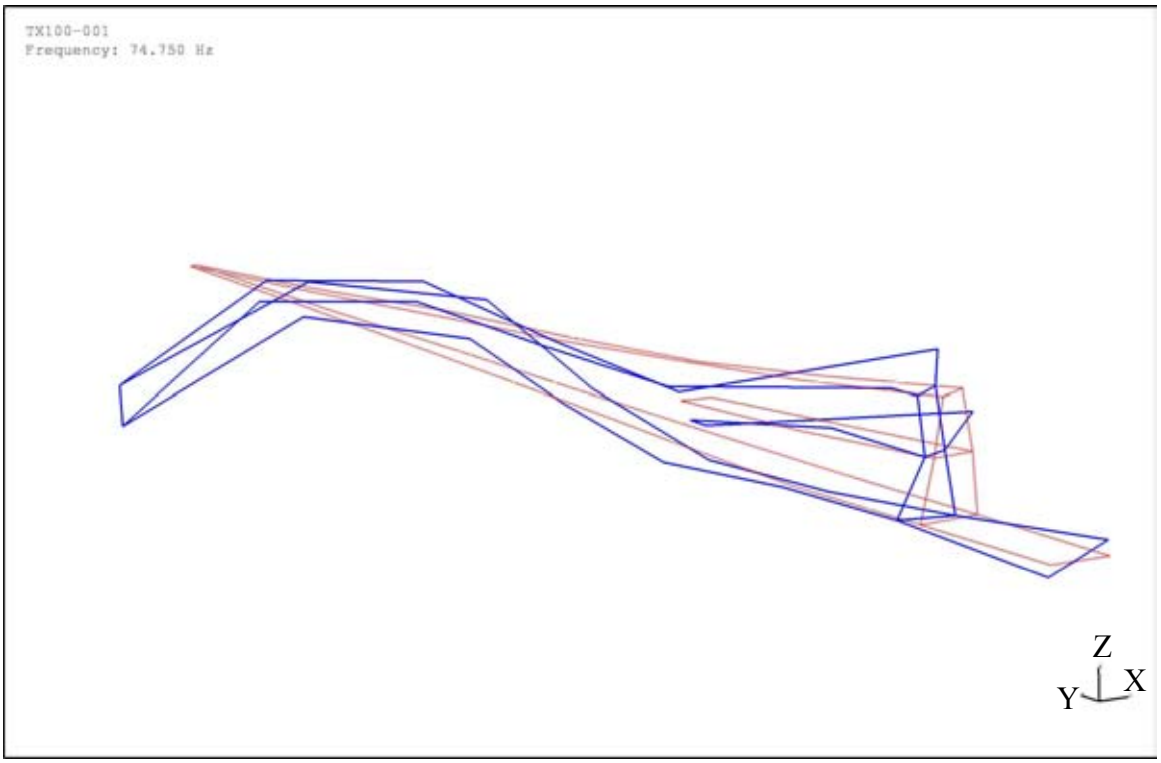

Figure A-9. Coupled Mode #1 (f = 75.13 Hz, ζ = 0.56 %) Blade Serial #TX-100-001

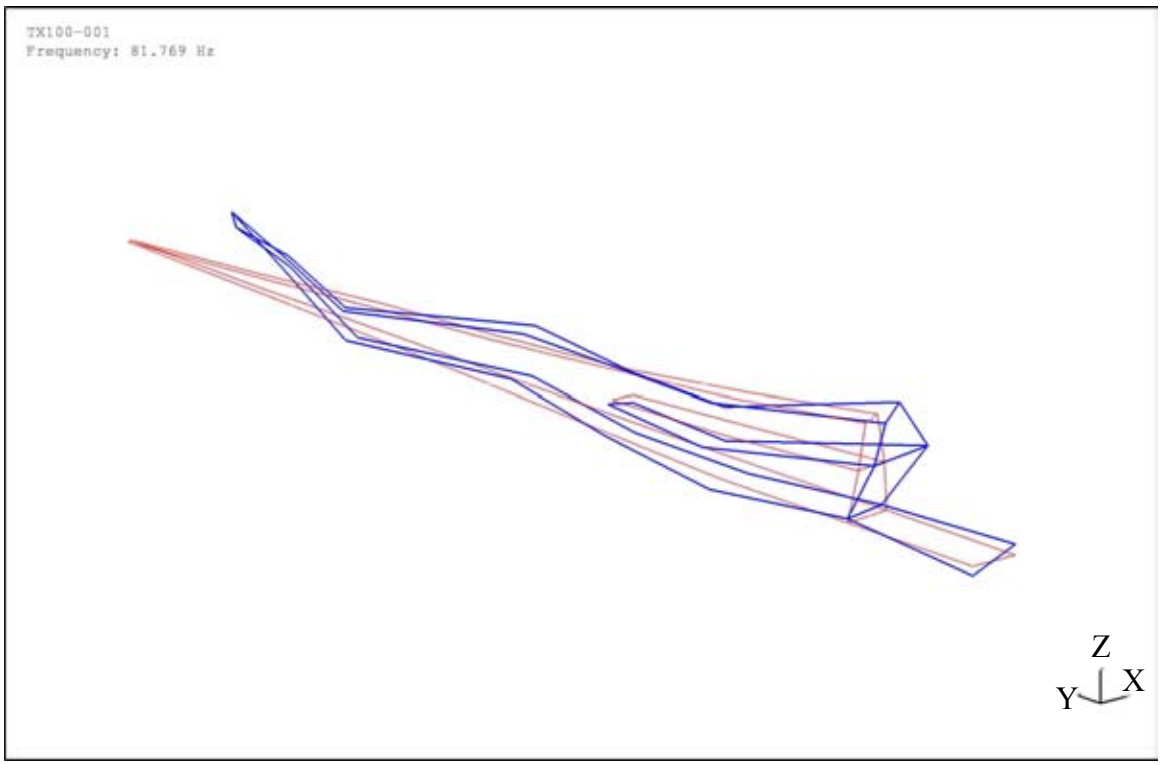

Figure A-10. Coupled Mode #2 (f =82.13 Hz, ζ = 0.50 %) Blade Serial #TX-100-001

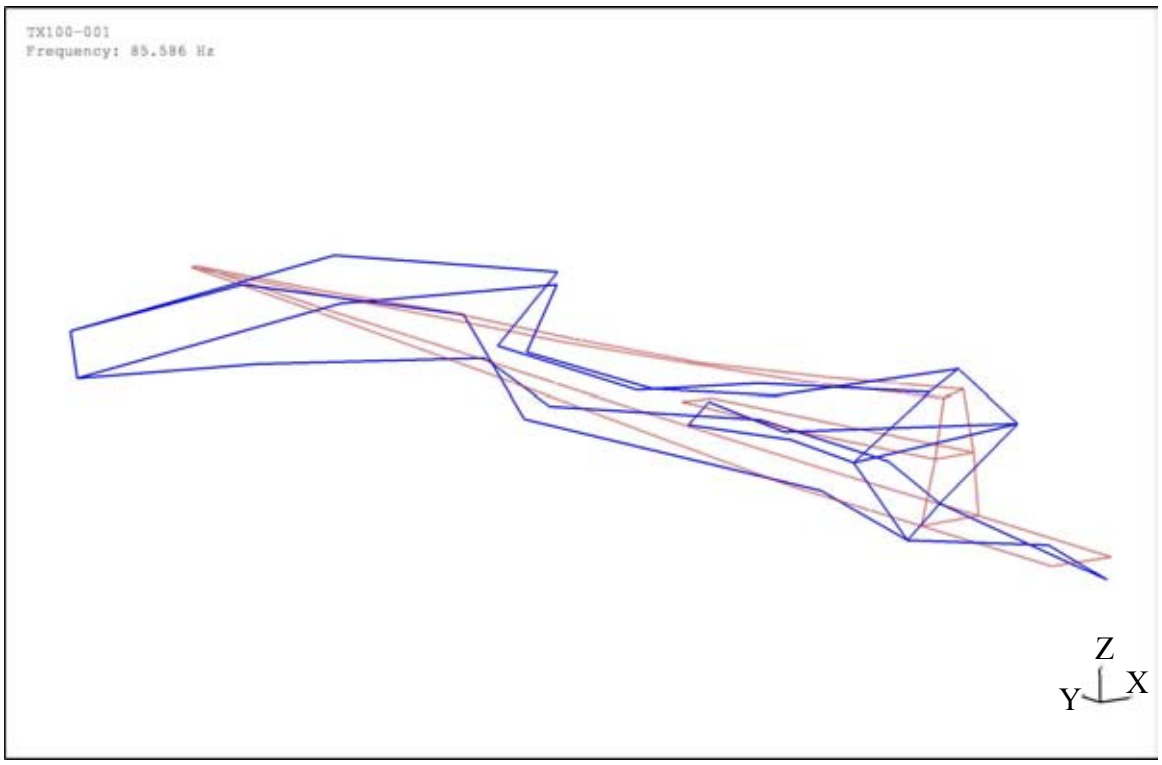

Figure A-11. Coupled Mode #3 (f = 85.59 Hz, ζ = 0.52 %) Blade Serial #TX-100-001

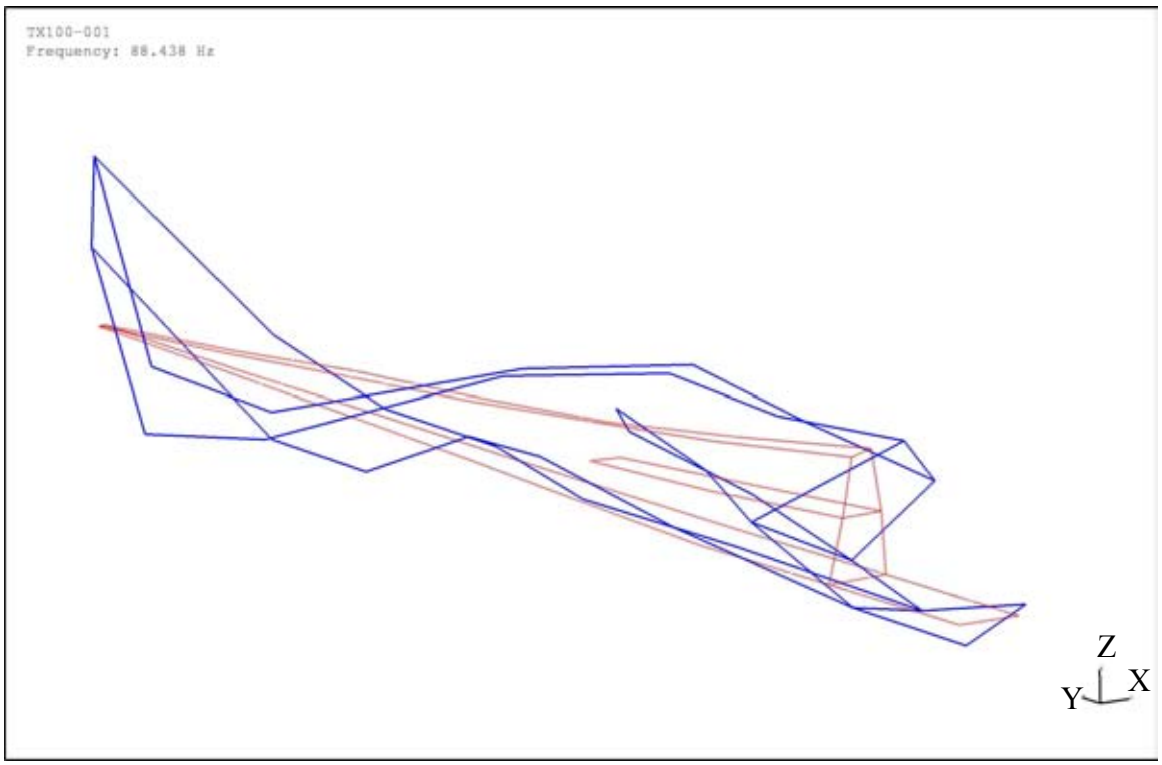

Figure A-12. Second Torsional Mode (f = 88.53 Hz, ζ = 0.80 %) Blade Serial #TX-100-001

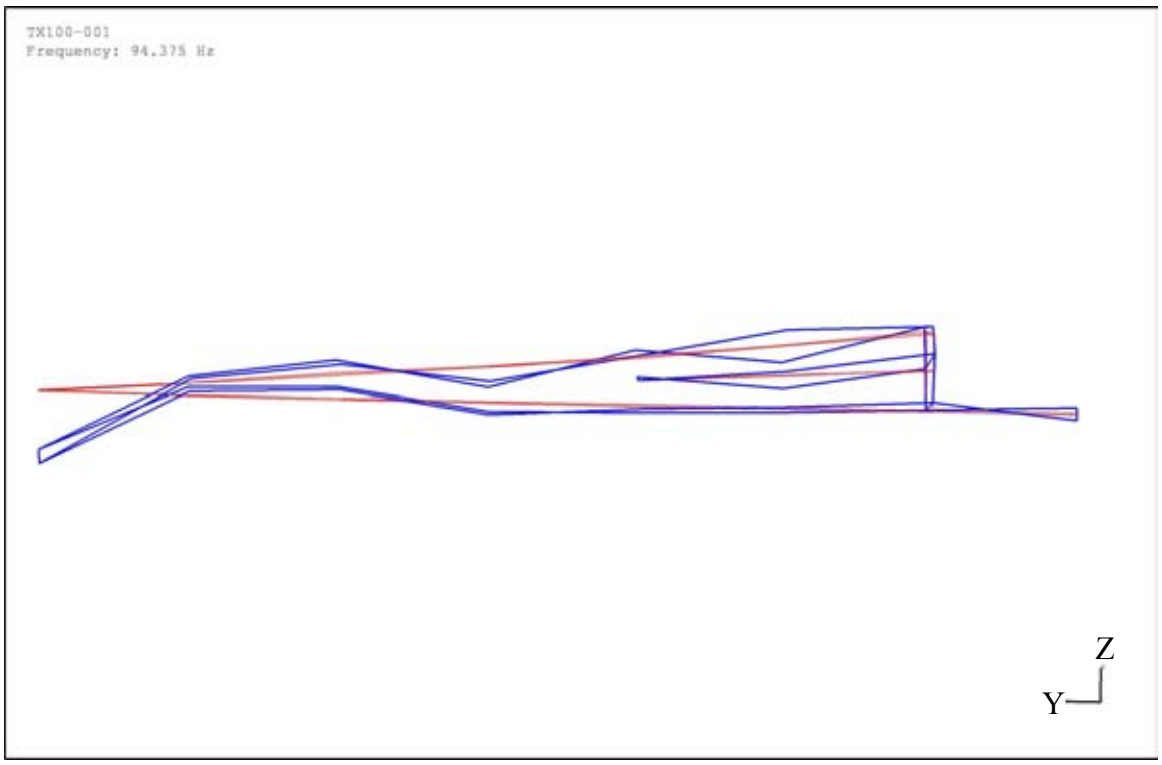

Figure A-13. Coupled Mode #4 (f = 95.06 Hz, ζ = 0.66 %) Blade Serial #TX-100-001

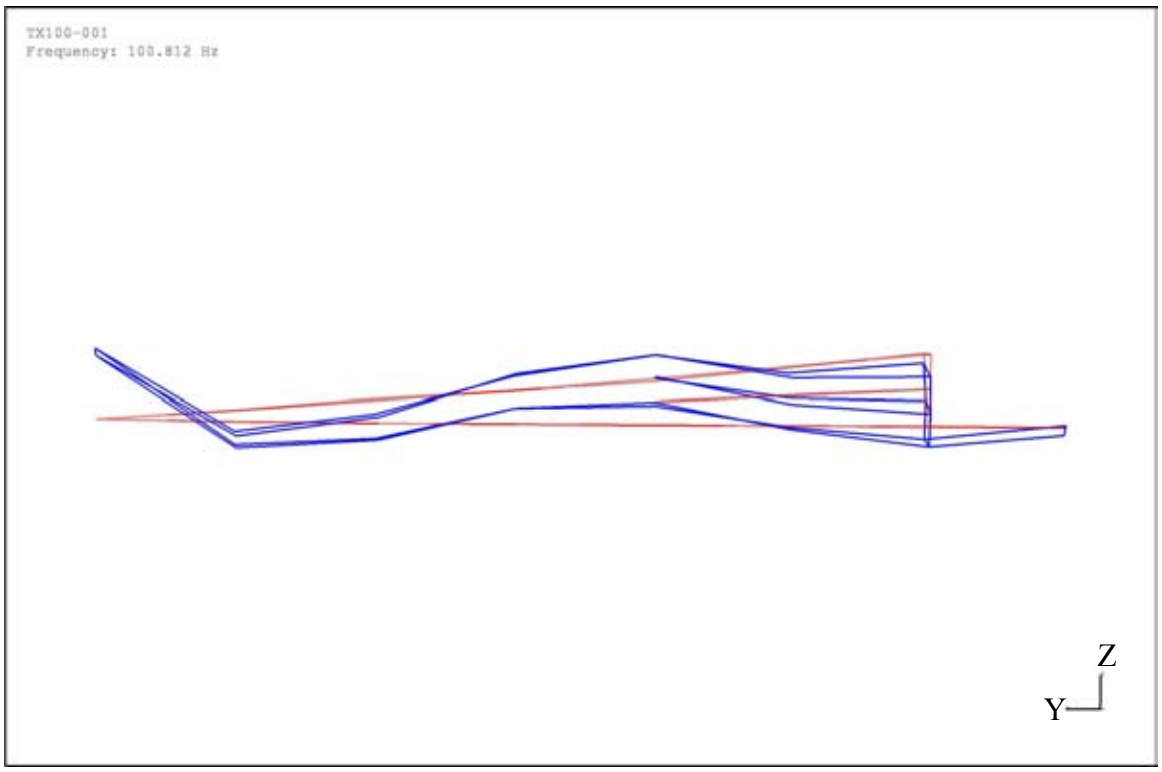

Figure A-14.Third Edgewise Mode (f = 101.04 Hz, ζ = 0.57 %) Blade Serial #TX-100-001

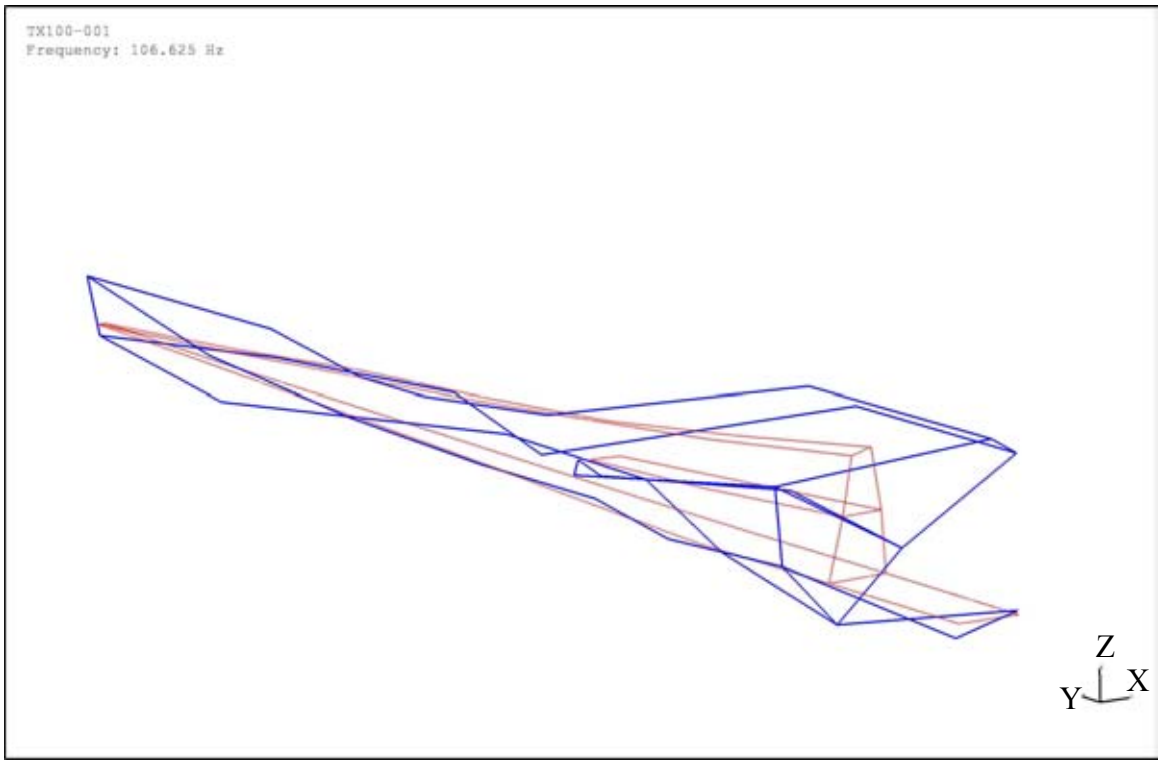

Figure A-15. Third Torsional Mode (f = 107.13 Hz, ζ = 0.73 %) Blade Serial #TX-100-001

Appendix B
Mode Shapes of Blade Serial #TX-100-003

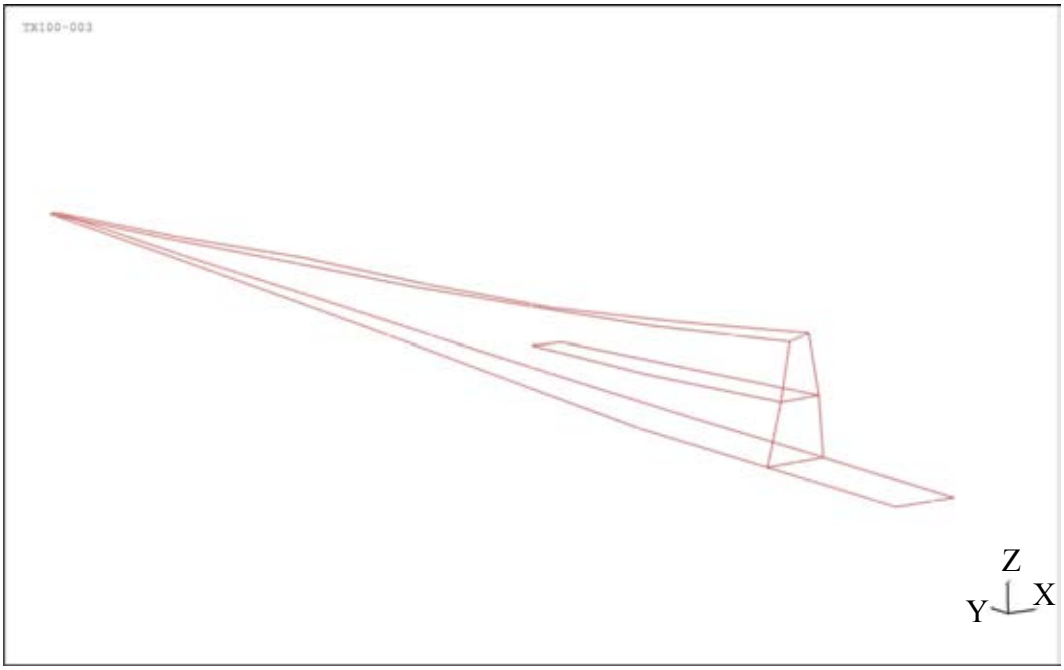

Figure B-1. Undeformed Blade Serial #TX-100-003

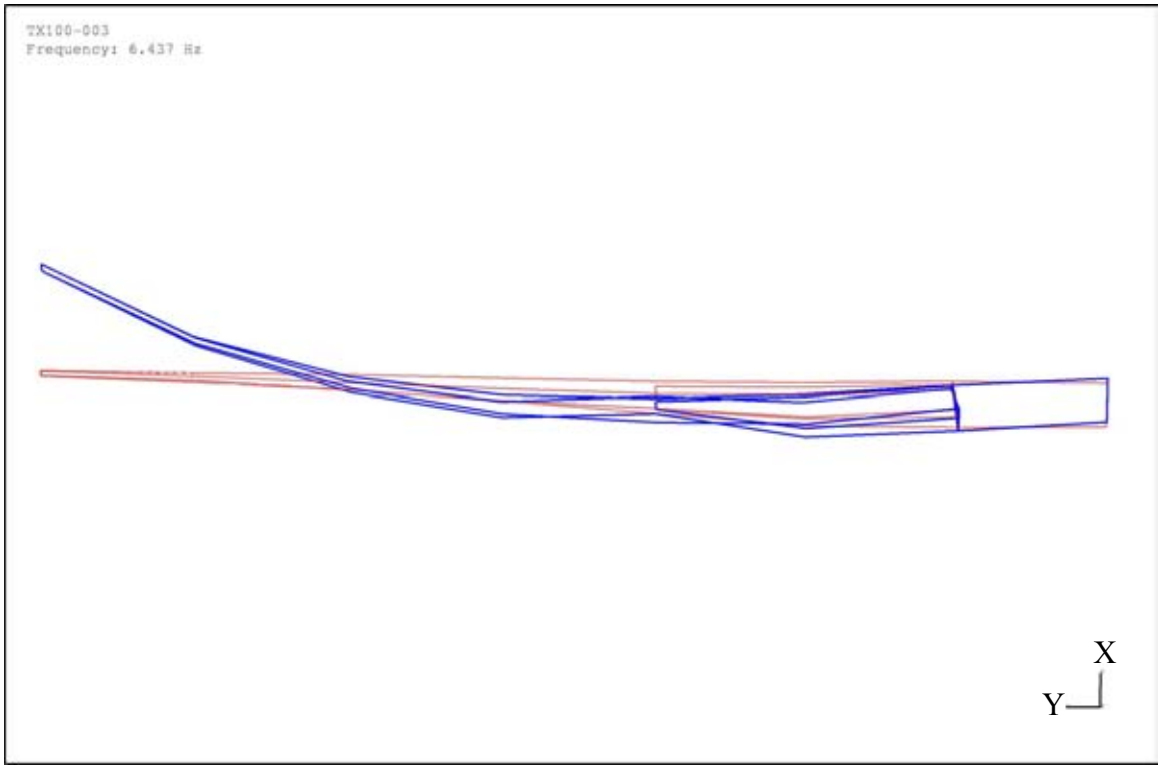

Figure B-1. First Flapwise Mode (f = 6.49 Hz, ζ = 0.20 %) Blade Serial #TX-100-003

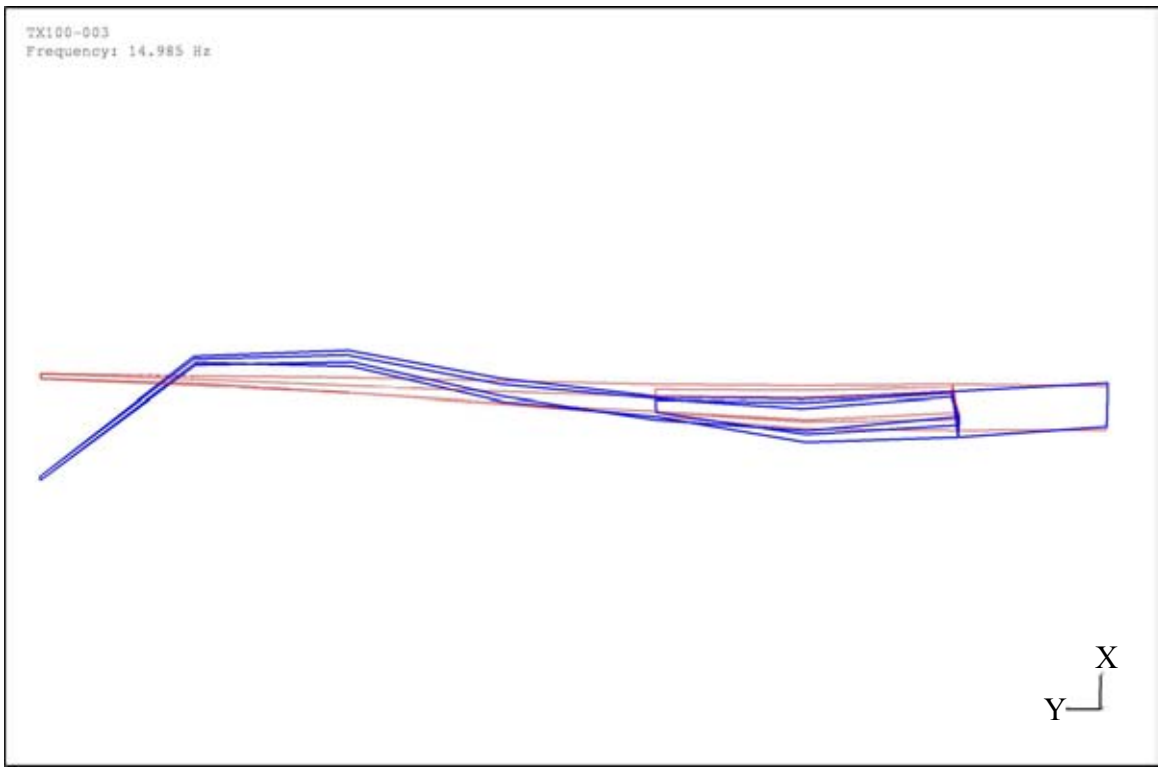

Figure B-2. Second Flapwise Mode (f = 15.14 Hz, ζ = 0.23 %) Blade Serial #TX-100-003

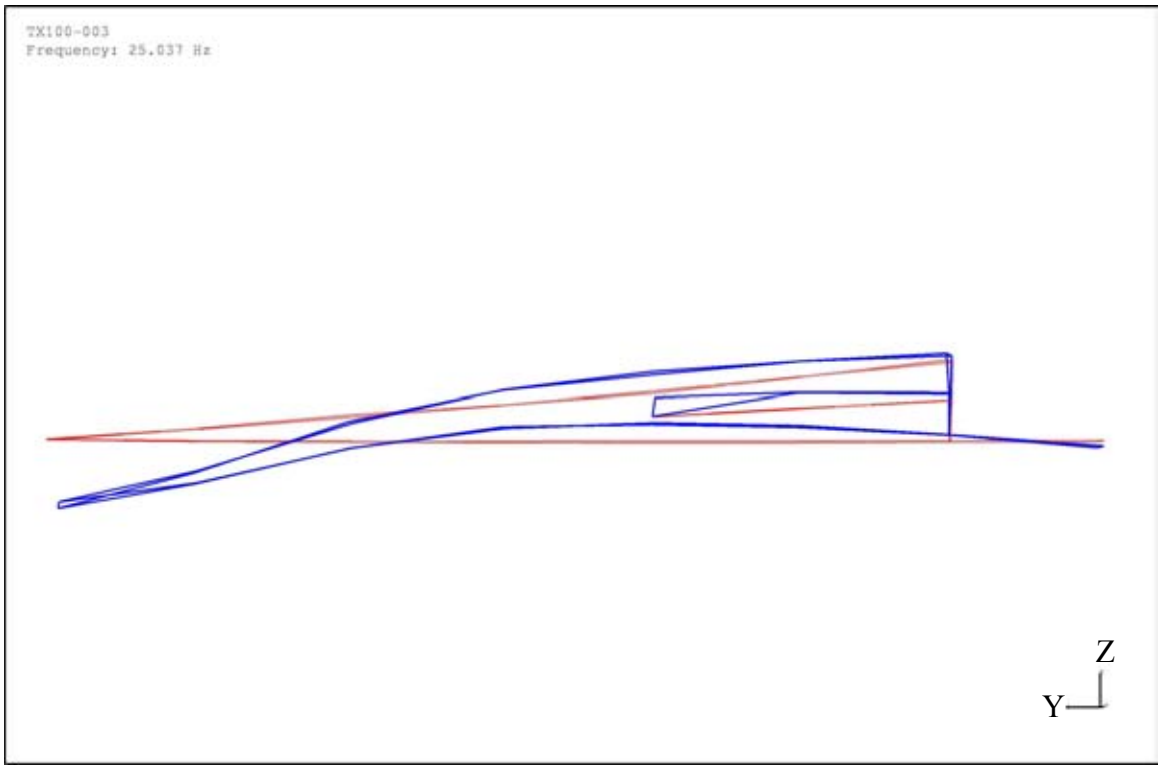

Figure B-3. First Edgewise Mode (f = 25.25 Hz, ζ = 0.34 %) Blade Serial #TX-100-003

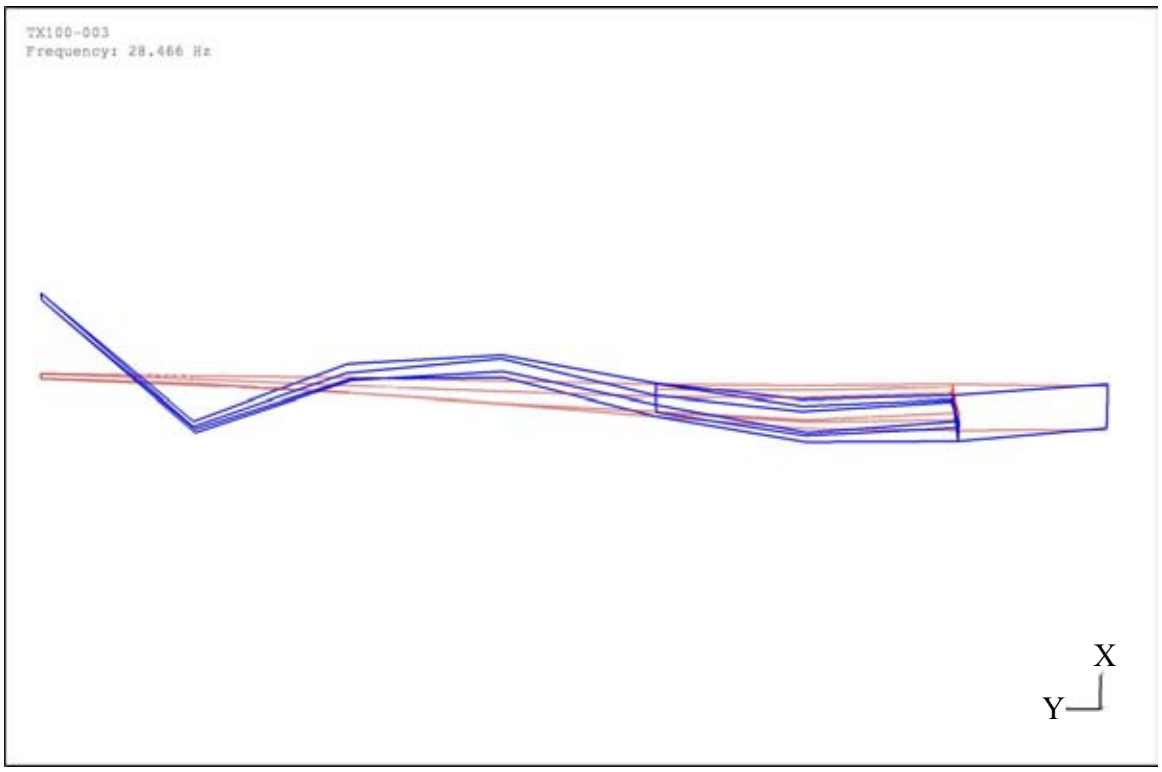

Figure B-4. Third Flapwise Mode (f = 28.94 Hz, ζ = 0.60 %) Blade Serial #TX-100-003

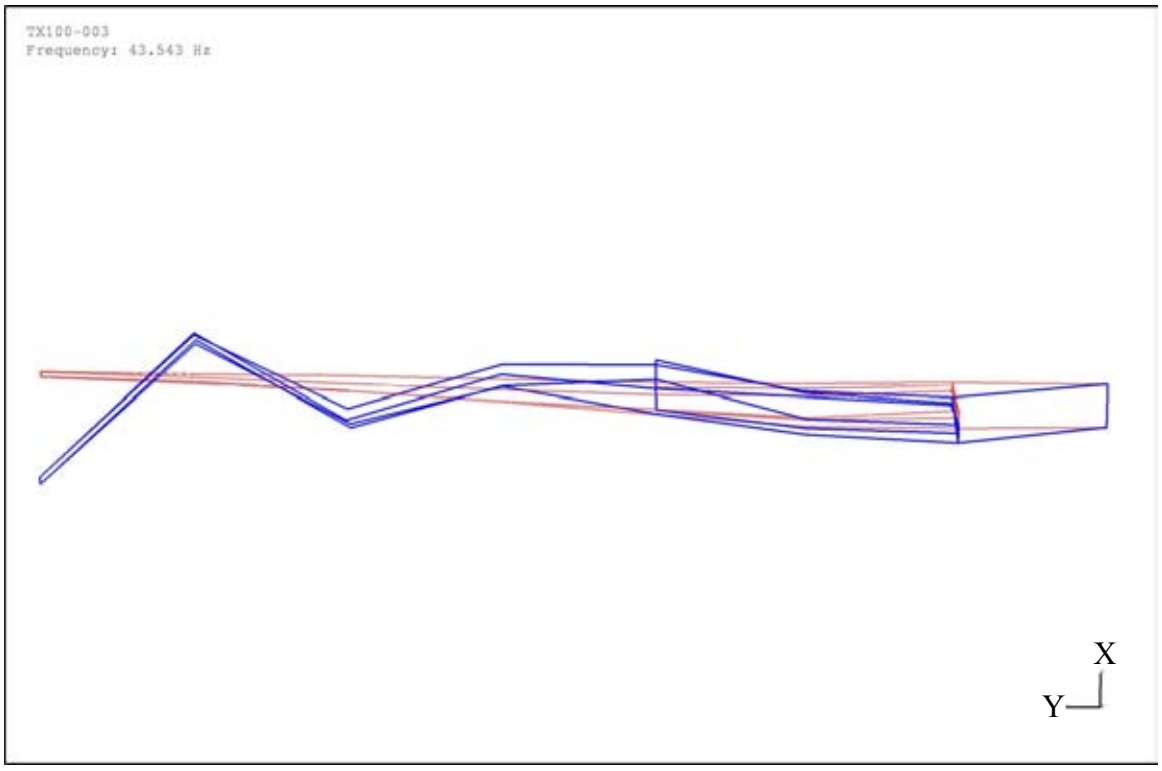

Figure B-5. Fourth Flapwise Mode (f = 43.92 Hz, ζ = 0.34 %) Blade Serial #TX-100-003

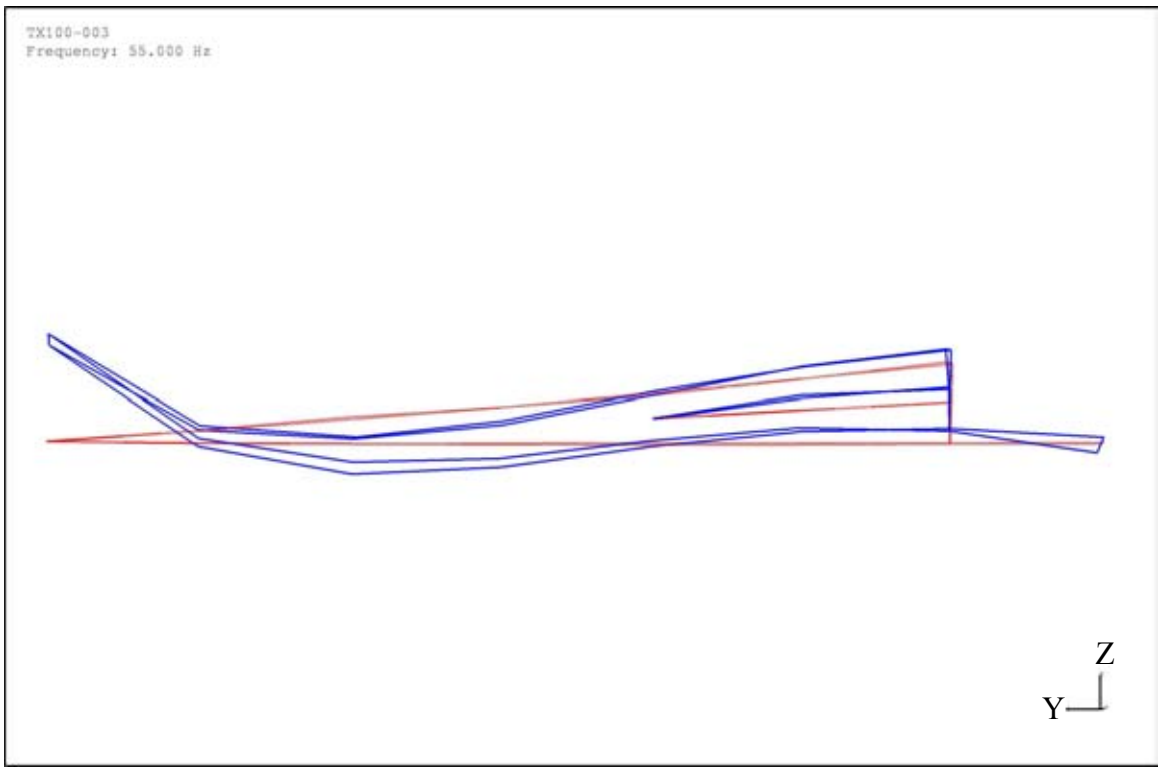

Figure B-6. Second Edgewise Mode (f = 55.31 Hz, ζ = 0.39 %) Blade Serial #TX-100-003

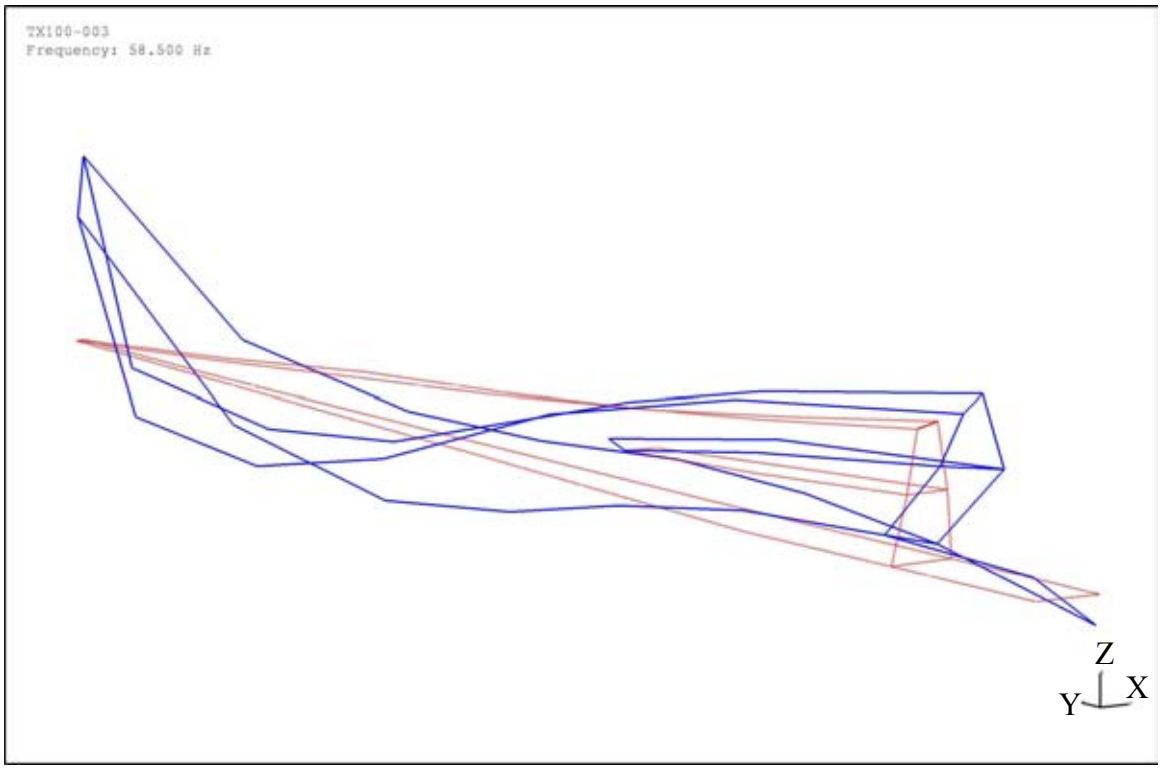

Figure B-7. First Torsional Mode (f = 58.82 Hz, ζ = 0.48 %) Blade Serial #TX-100-003

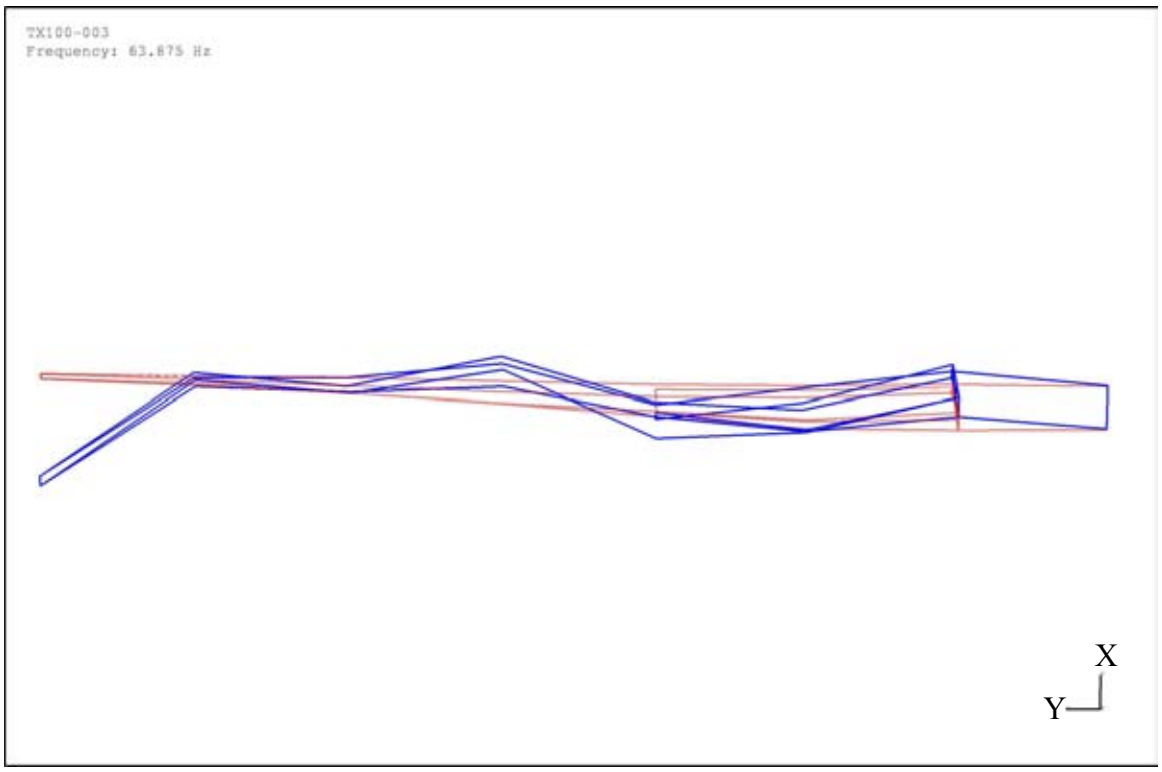

Figure B-8. Fifth Flapwise Mode (f = 64.20 Hz, ζ = 0.31%) Blade Serial #TX-100-003

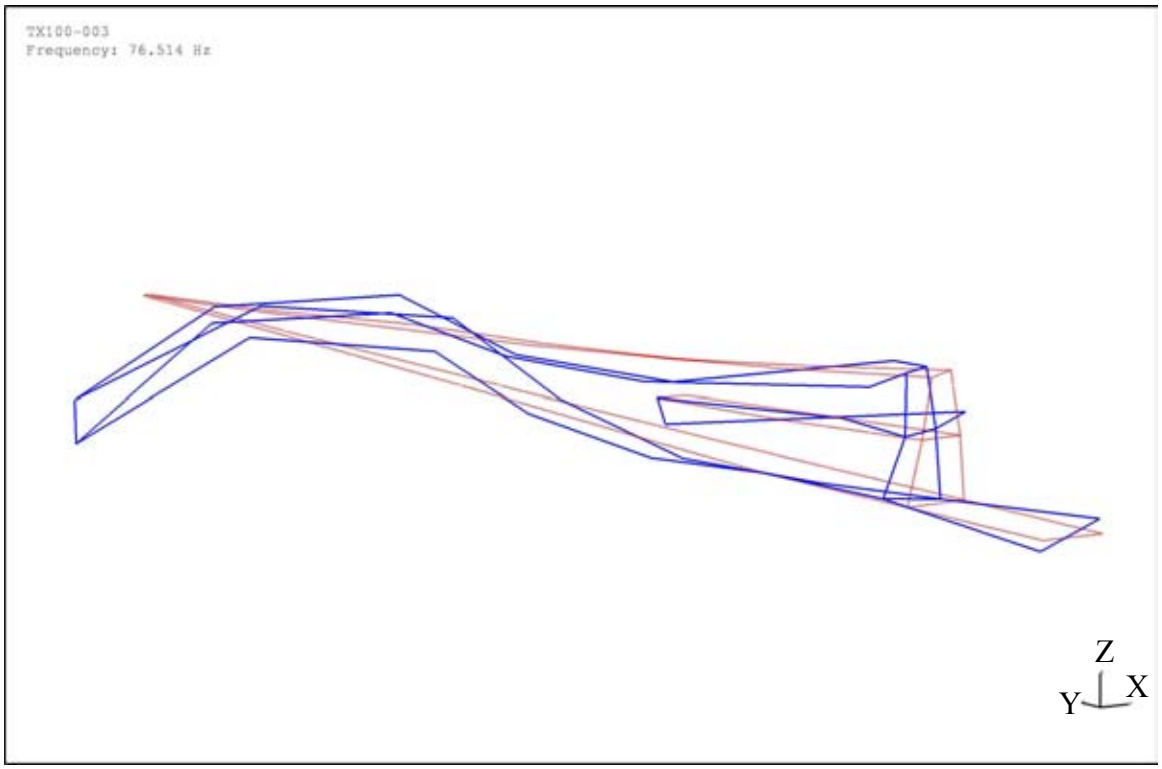

Figure B-9. Coupled Mode #1 (f = 76.39 Hz, ζ = 0.58 %) Blade Serial #TX-100-003

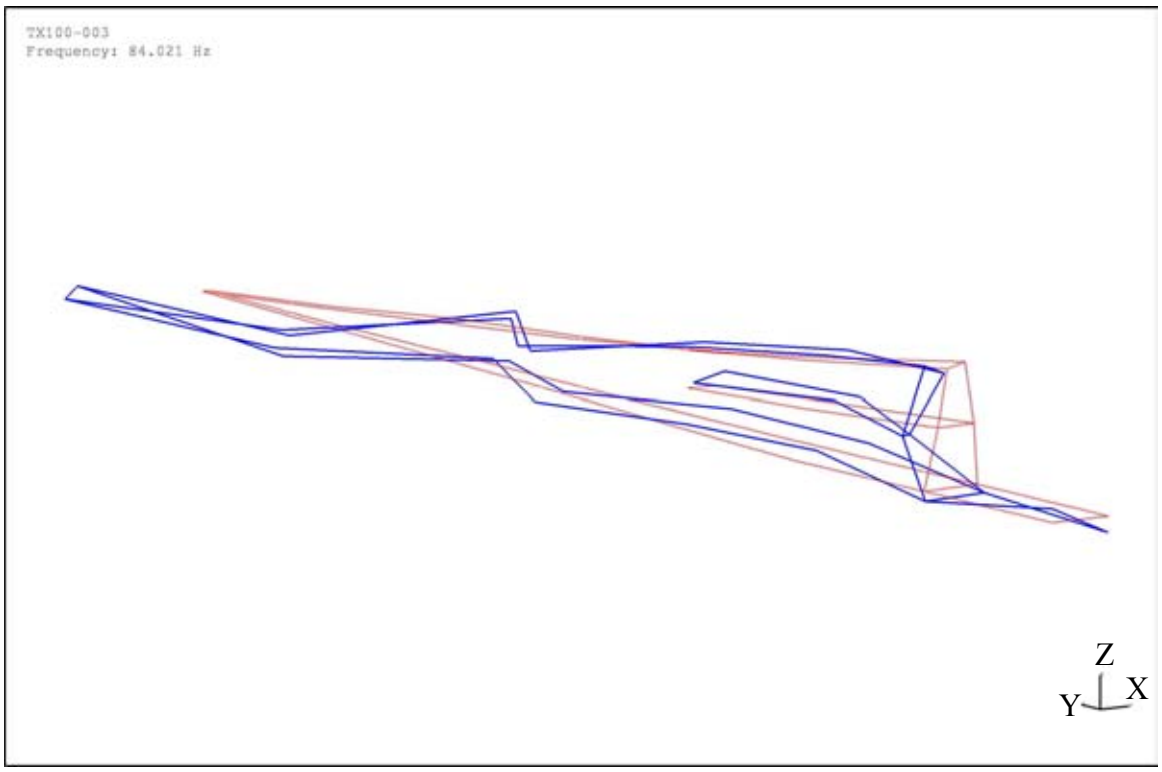

Figure B-10. Coupled Mode #2 (f = 83.92 Hz, ζ = 0.64 %) Blade Serial #TX-100-003

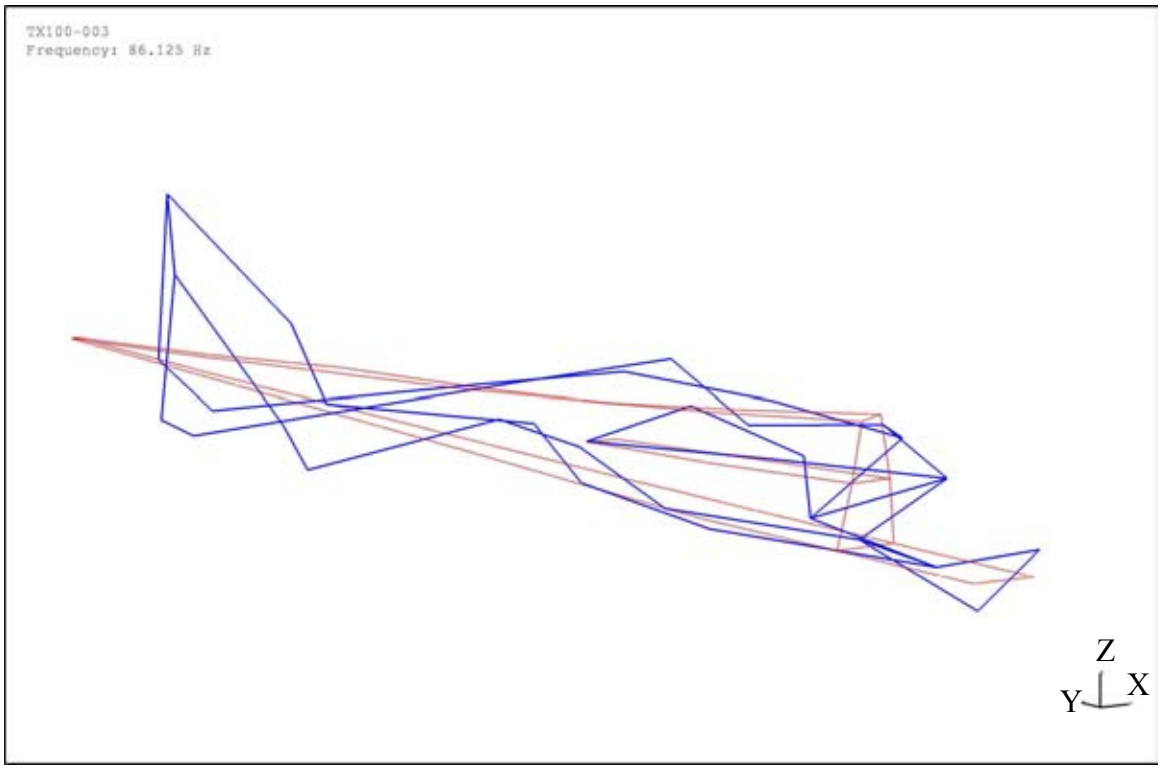

Figure B-11. Coupled Mode #3 (f = 86.13 Hz, ζ = 0.51 %) Blade Serial #TX-100-003

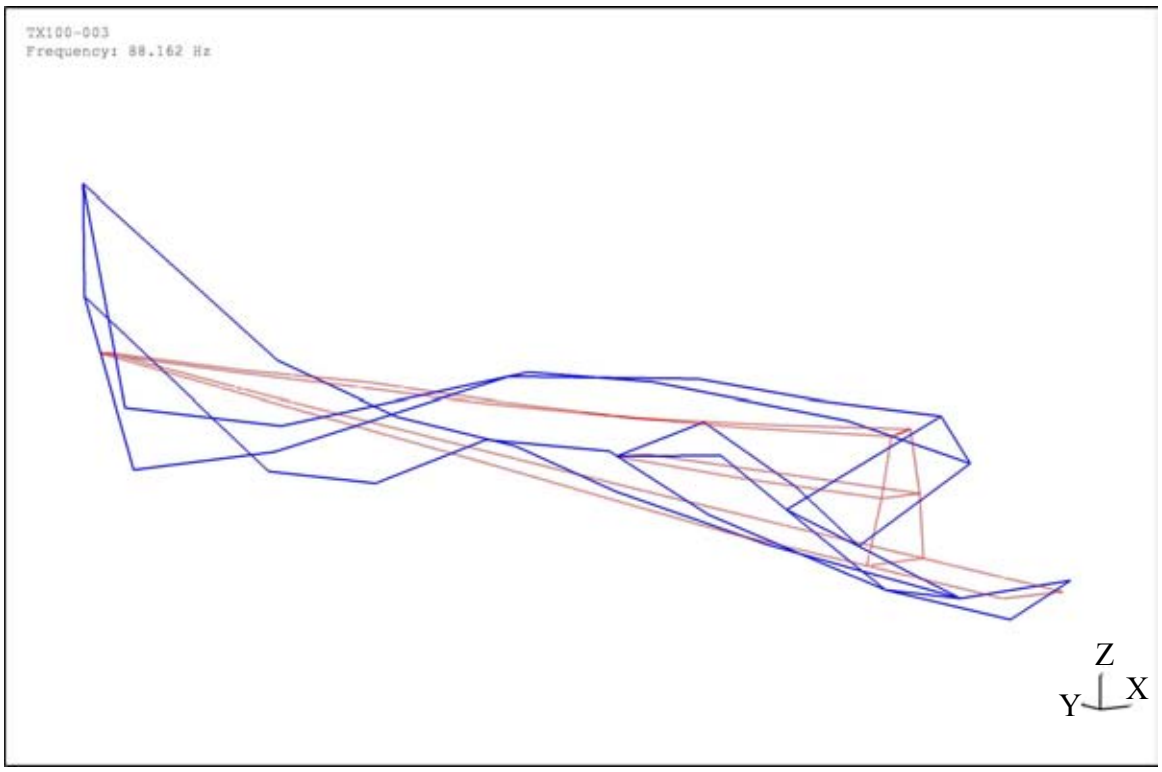

Figure B-12. Second Torsional Mode (f = 87.94 Hz, ζ = 0.56 %) Blade Serial #TX-100-003

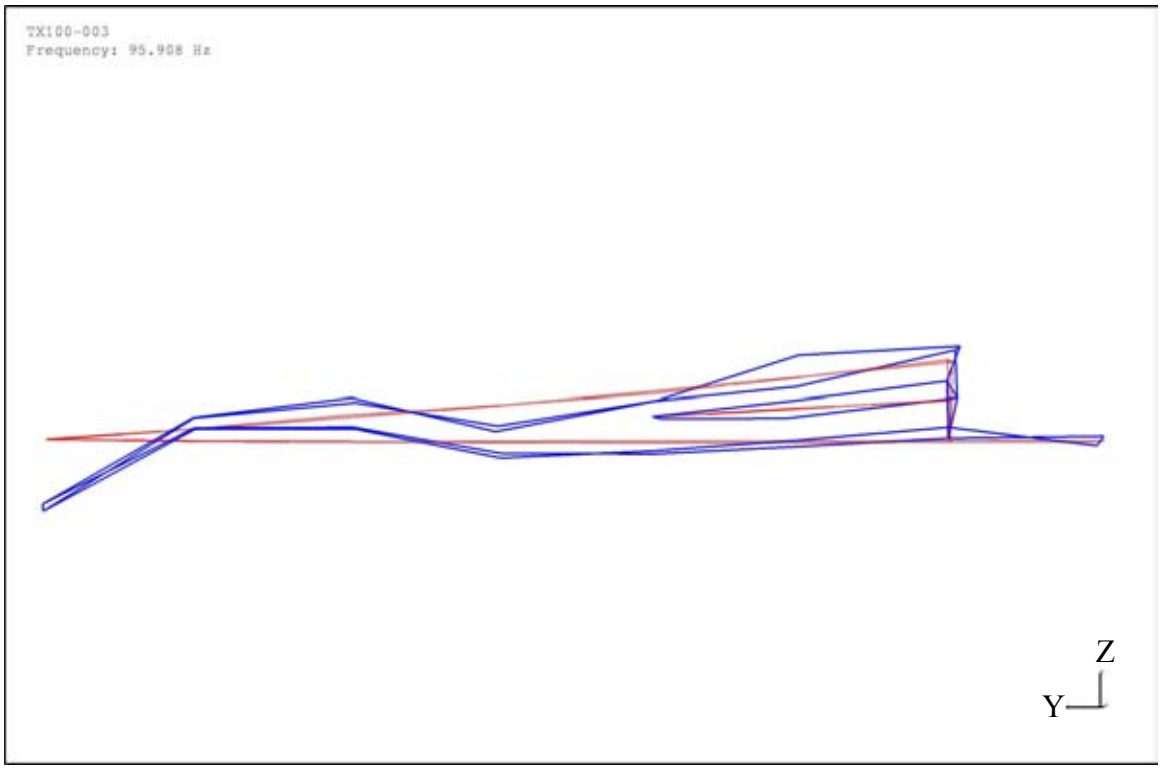

Figure B-13. Coupled Mode #4 (f = 96.81 Hz, ζ = 0.58 %) Blade Serial #TX-100-003

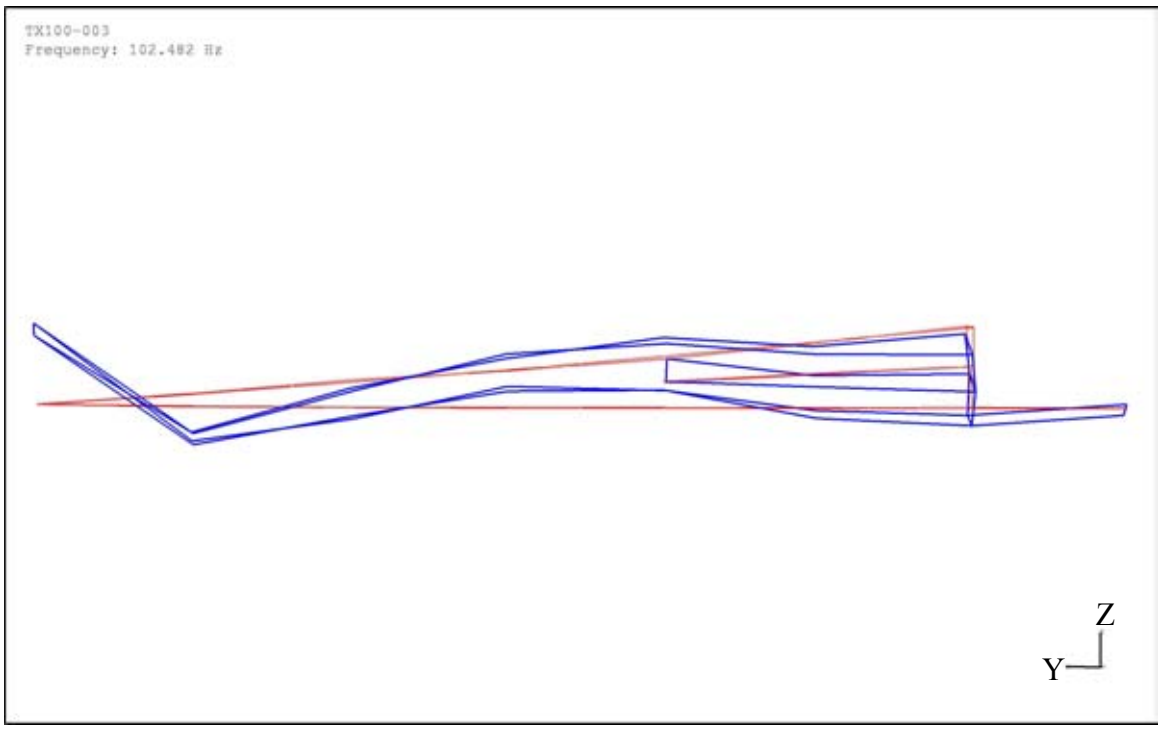

Figure B-14. Third Edgewise Mode (f = 102.75 Hz, ζ = 0.47 %) Blade Serial #TX-100-003

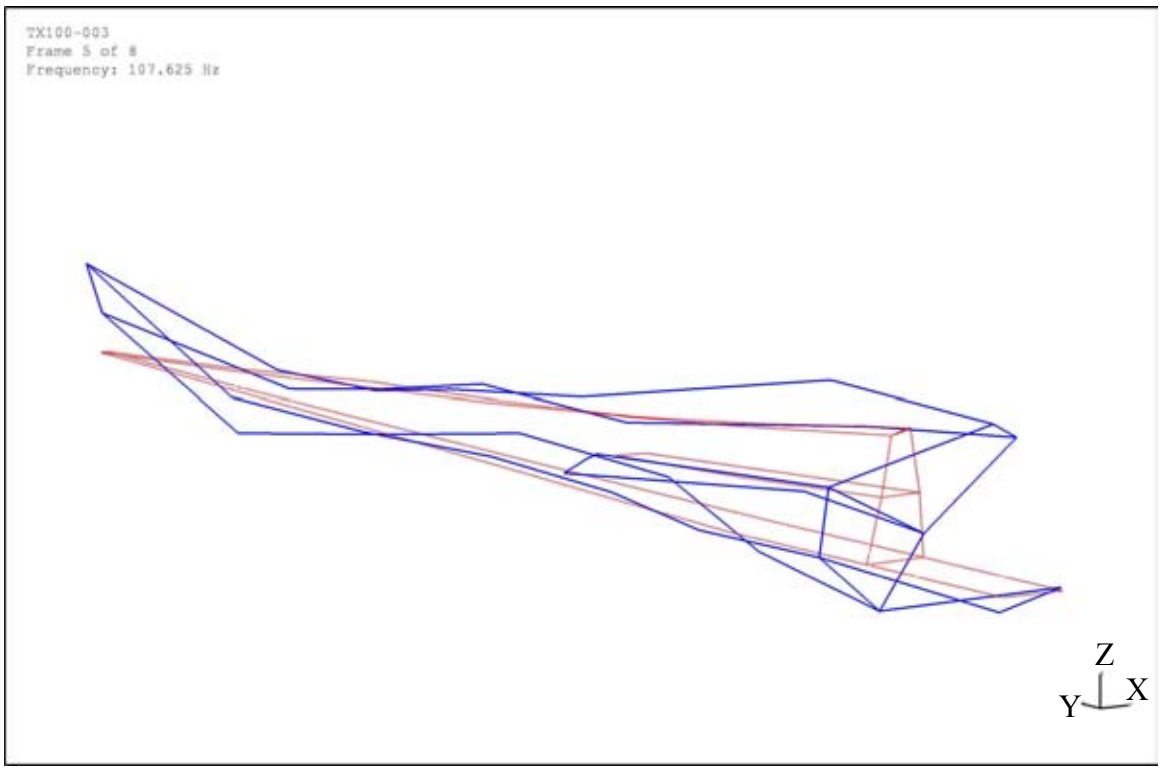

Figure B-15. Third Torsional Mode (f = 107.81 Hz, ζ = 0.90 %) Blade Serial #TX-100-003

Appendix C
Accelerometer Placement Procedure

This appendix details the procedure developed to instrument the wind turbine blade with an array of 68 accelerometers. The result is an instrumented blade with 34 accelerometer placement locations that are parallel to both the x- and z-axis to the implied Cartesian coordinate system's origin located at the hub of the wind turbine blade. The coordinate system at the base of the hub is seen in Figure C-1 when the trailing edge is pointed up.

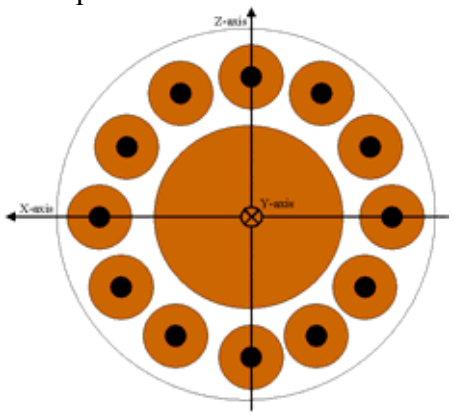

Figure C-1. Coordinate System at Hub

The wind turbine blade must be aligned to the global Cartesian coordinate system defined by the ground to accurately mount the accelerometers on their desired axis. Suspend the blade such that the blade's hub, or z-axis, is perpendicular to the ground, i.e. perpendicular to the global y-axis as seen in Figure C-2.

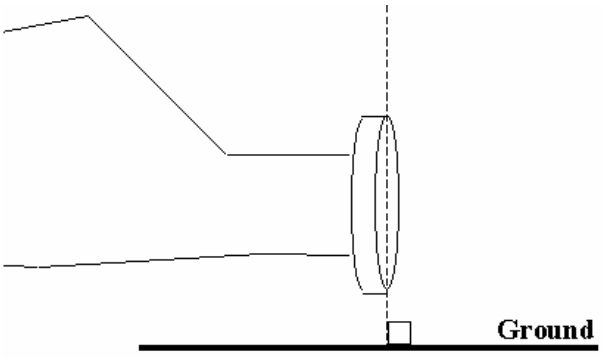

Figure C-2. Alignment of Wind Turbine Blade with Ground

Then rotate the blade along the y-axis such that the z-axis is parallel to the global z-axis with the trailing edge up as seen below. Here the blade's z-axis is to the left of the global z-axis which is denoted as z'. Therefore, the blade's trailing edge would be rotated to the right in order to align axis as seen in Figure C-3.

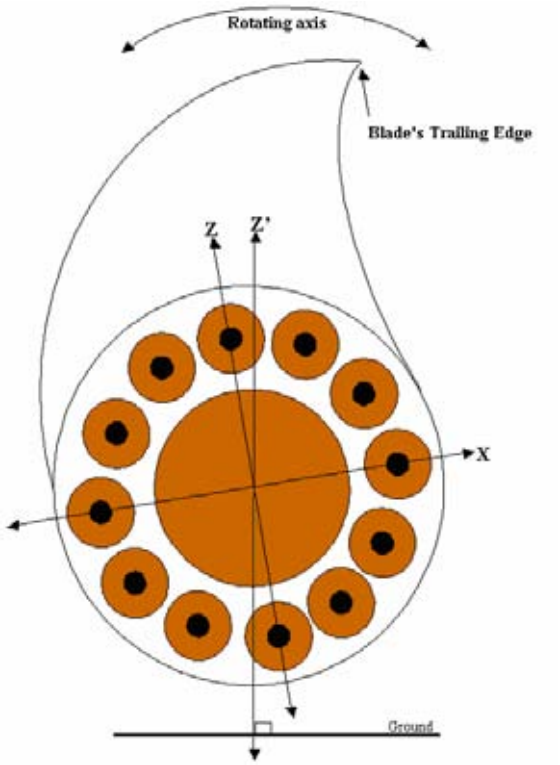

Figure C-3. Rotating Alignment of Wind Turbine Blade

Chalk a line from the x-axis at the hub to the middle of the blade's tip when the blade flattens out parallel to the z-axis. This line will later be referred to as line 1 as seen in Figure C-4.

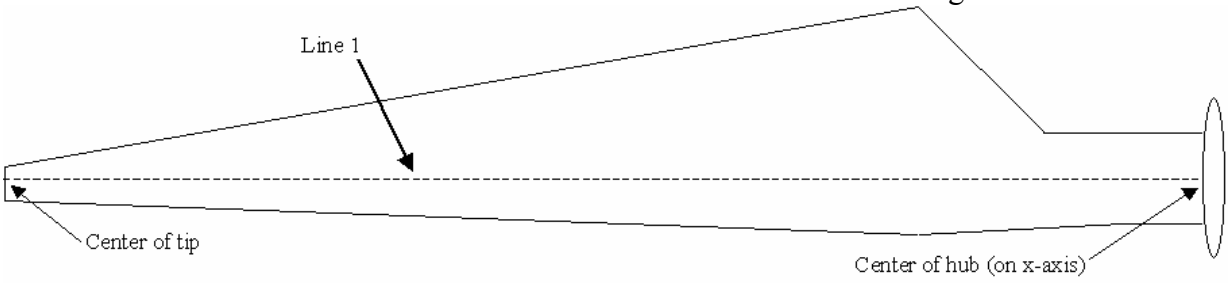

Figure C-4. Creation of Line 1

Chalk a line that is 3 ¾ inches from and parallel to the trailing edge from the highest point of the blade to the tip as seen below. This will be referred to as line 3 as seen in Figure C-5.

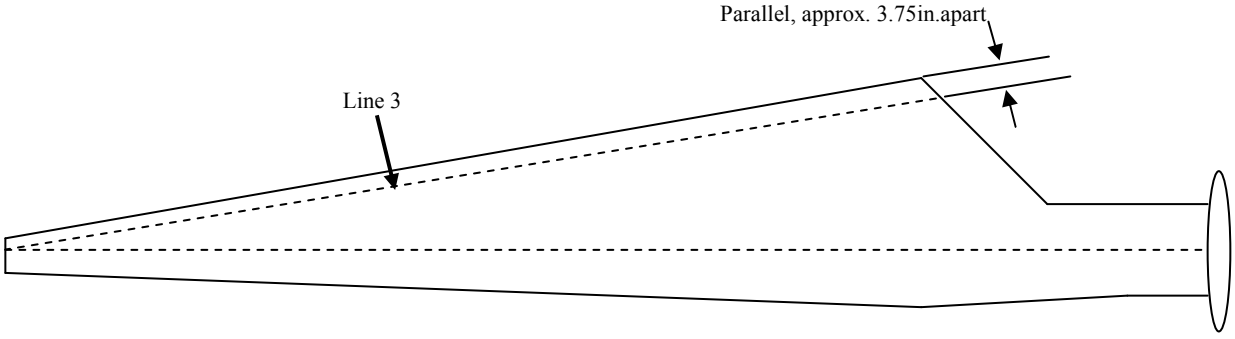

Figure C-5. Creation of Line 3

Chalk a line that is perpendicular to line 1 to the highest point of the trailing edge, which will be referred to as line 20 as seen in Figure C-6.

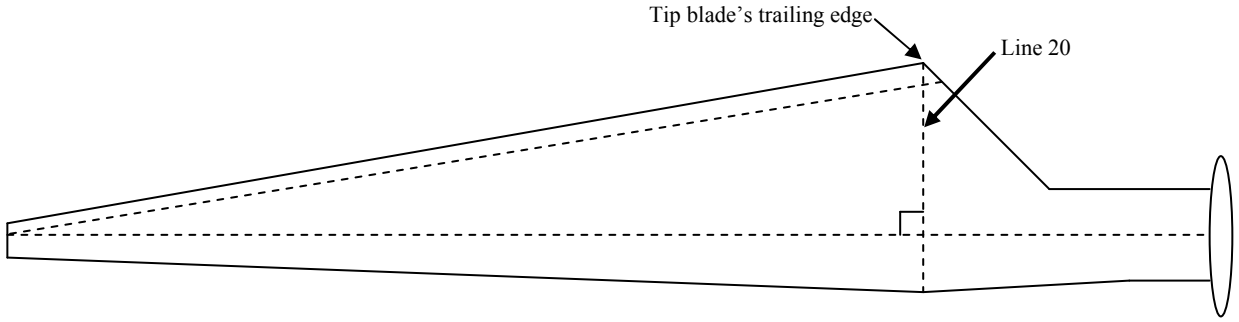

Figure C-6. Creation of Line 20

Then measure the distance from where lines 1 and 3 interest to where lines 1 and 20 intersect. This distance is to be section into six equally spaced parts, a distance of 'y' apart, along line 1. Mark these points with tape or chalk. Chalk five separate lines that are perpendicular to line 1 at each of the marked points. These lines should be parallel to each other as well as to line 20 as seen below, noting the respective labels of these lines as seen in Figure C-7.

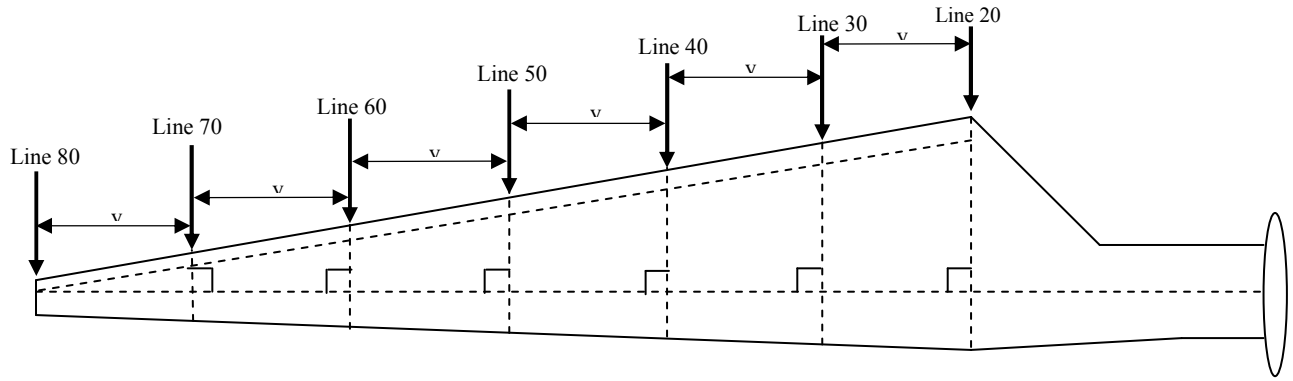

Figure C-7. Creation of Line 30, 40, 50 and 60

Determine the midpoint along line 20 between where lines 1 and 3 intersect it. Chalk a line from that point to where lines 1 and 3 intersect near the tip of the blade. This line should create equal segments between lines 1 and 3 along lines 20, 30, 40, 50 and 60. This can be seen below whereas length z1 and z2 are equal to their respective counterparts as seen in Figure C-8.

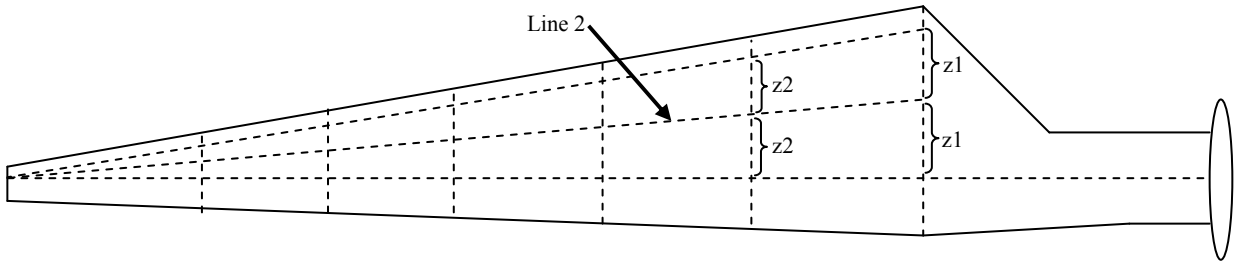

Figure C-8. Creation of Line 2

Measure the distance of each segment along line 1. This should be some distance 'y'. Mark one point along line 1 between line 20 and the hub of the blade that is the same distance, 'y' from line 1. Chalk line 10 at this new point that is perpendicular to line 1 as seen in Figure C-9.

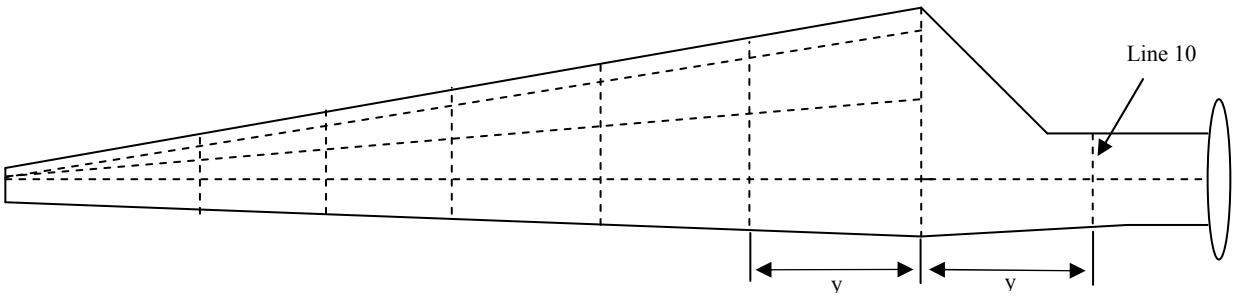

Figure C-9. Creation of Line 10

Thereafter create a similar pattern on the other side of the wind turbine blade in the same fashion. All vertical lines, i.e. lines parallel to line 20, should align with the lines created on the other side of the blade.

The locations of where the accelerometers are to be placed are represented in Figure C-10 as black spots. These locations are at the point of intersection of their respective lines, noting that accelerometers will not be placed at every intersection point.

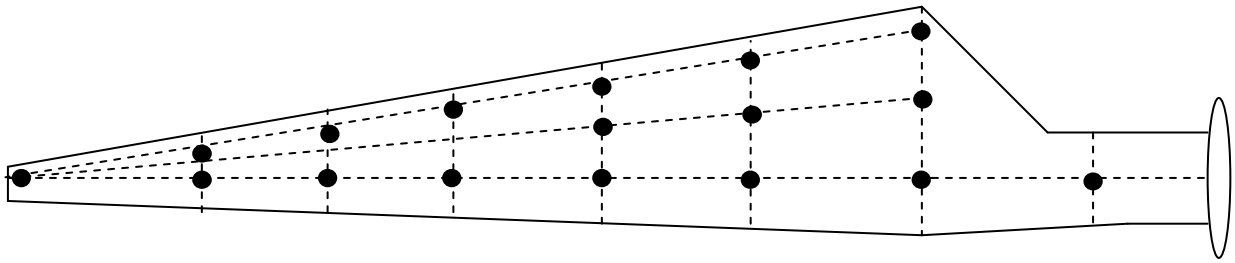

Figure C-10. Accelerometer Locations

For ease of analysis, each location is to be numbered. To determine the number location, simply add the number lines that intersect at that particular intersection. For instance, the point where line 1 and line 10 intersect creates an accelerometer location that is number 11 (i.e. line 1 + line 10 = point 11, which is located at the base of the hub). The convex side of the blade is where the positive x-axis is and this will be the side where the double-digit accelerometer locations are as seen in Figure C-11.

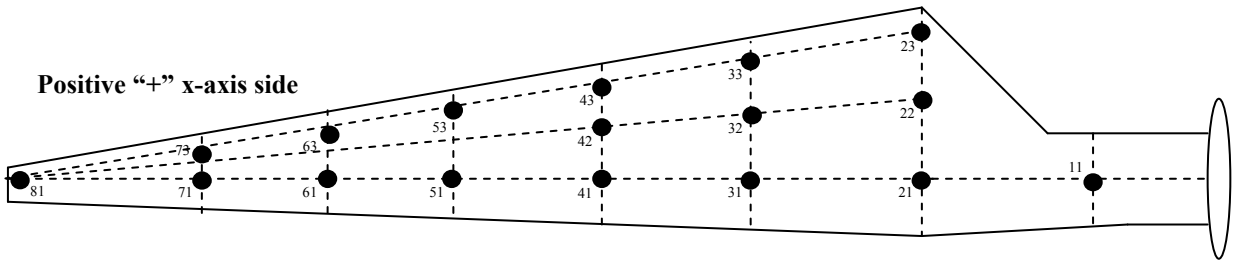

Figure C-11 Accelerometer Location Numbering Scheme for Convex Side

The concave side of the blade is where the negative x-axis is and this will be the side where the triple-digit accelerometer locations are. The difference in numbering of these locations is that these numbers have 100 added to them as seen in Figure C-12.

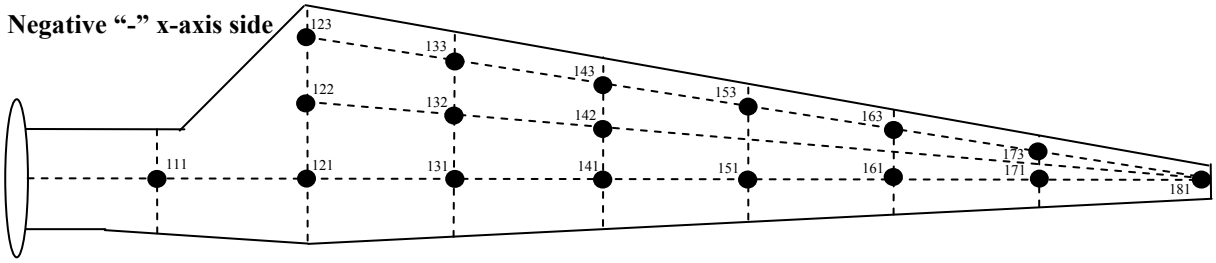

Figure C-12. Accelerometer Location Numbering Scheme for Concave Side

Clean the blade at each accelerometer location, approximately a four by four inch region with the center at the intersection point. A three-inch strip of aluminum tape is to be placed there, again with the center at the intersection point. To ease clean up, fold one corner of the tape inward. A phenolic block is to be used to release any air bubbles that may occur. It is of extreme importance that the tape is completely and smoothly bonded to the blade so additional frequencies are not created in the process. The purpose of the tape is to not damage the finish of the blade. This can be seen in Figure C-13.

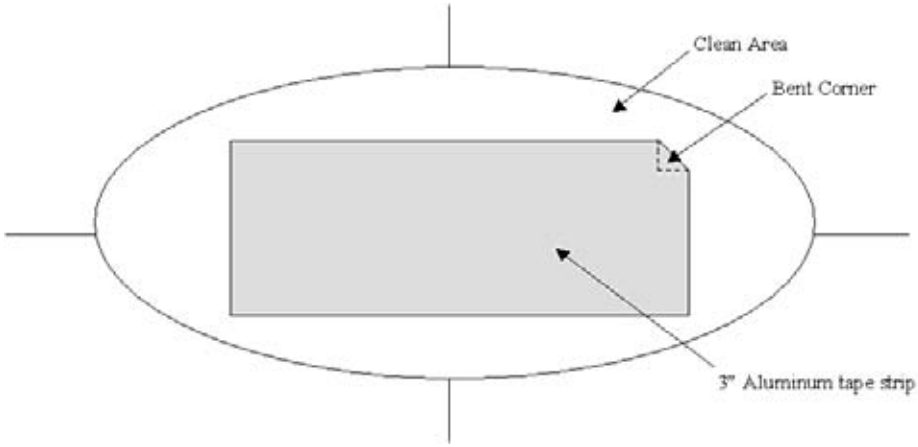

Figure C-13. Taping Process

Using a marker, redraw the lines only over the tape so the exact accelerometer placement locations are clearly defined. It should look as if there is a "+". The tape location can also be numbered for easy identification as seen in Figure C-14.

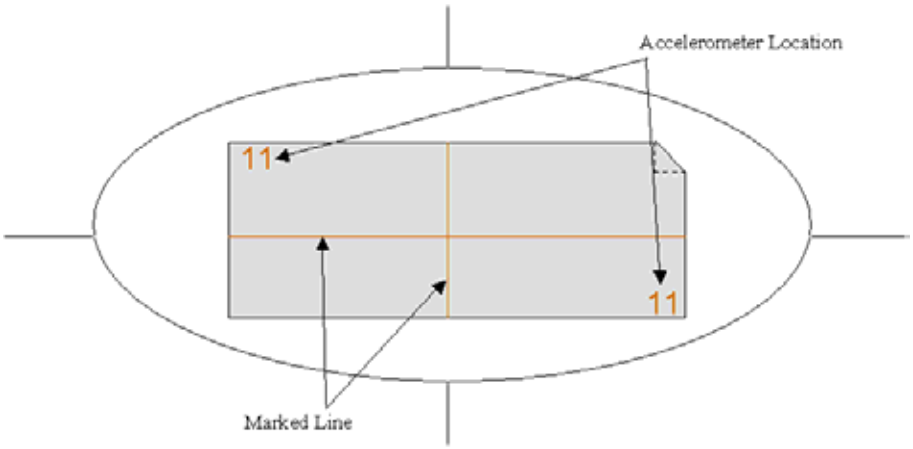

Figure C-14. Tape Identification Process

Using dental cement, bond a phenolic block at the "+" such that it is both perpendicular and parallel to the ground, i.e. the coordinate system defined earlier at the hub since the blade should be still aligned with the ground as seen in Figure C-15. A leveler was used for this process. Although the ideal mounting alignment is 0º with the respective axis, most were within 3º settling alignment with the dental cement. Remove any excess dental cement on the top and the side away from the blade for mounting the accelerometers.

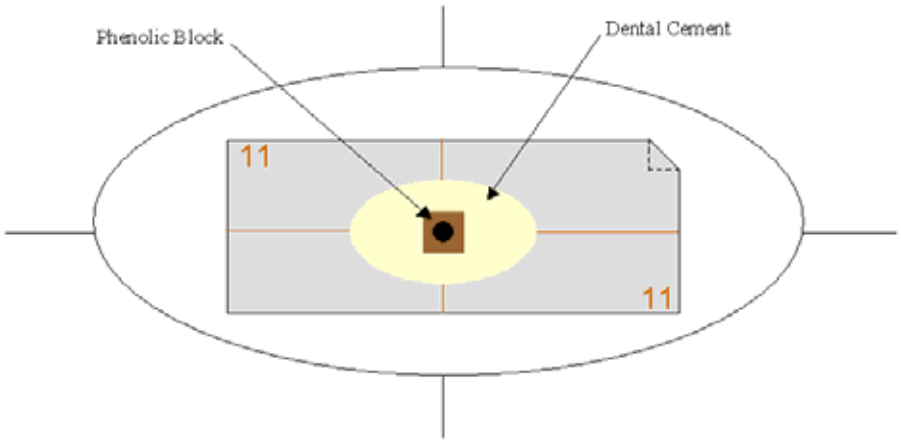

Figure C-15. Phenolic Block Attachment

Glue the two accelerometers on the phenolic block using M-Bond Adhesive, with one accelerometer parallel to the x-axis and the other parallel to the z-axis as seen in Figure C-16. To ensure, mounting accuracy, re-measure the angle of each mounted accelerometer. In the case that an accelerometer possesses a settling alignment greater than 3º, remove the accelerometer and/or phenolic block if needed and remount items.

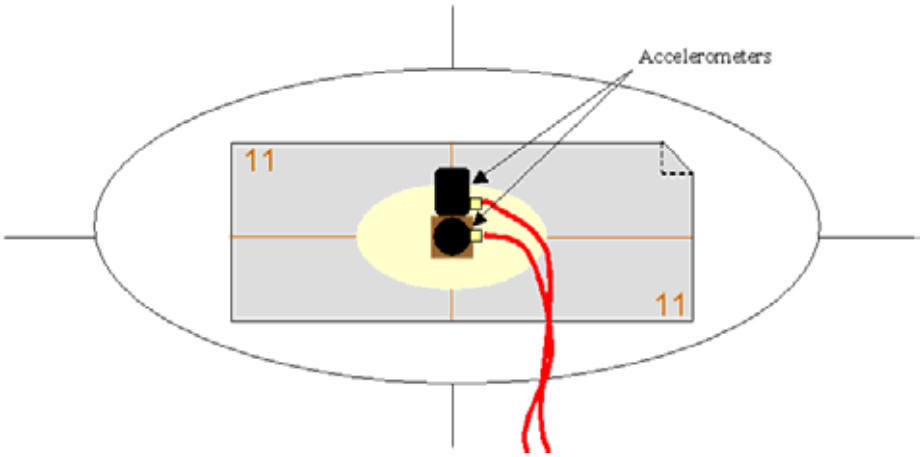

Figure C-16. Bonding Accelerometers

Since this test is preformed in a free-free condition. The blade is to be suspended with bungee cords. When using two nylon straps, one is positioned at one side of the blade's CG while the other is positioned at the other side. The CG should already be marked with a circle and a "+" sign on the blade. This setup ensures that the blade is stable during testing. Being sure to place the nylon straps several feet apart and clear of any accelerometers and cables as seen in Figure C-17.

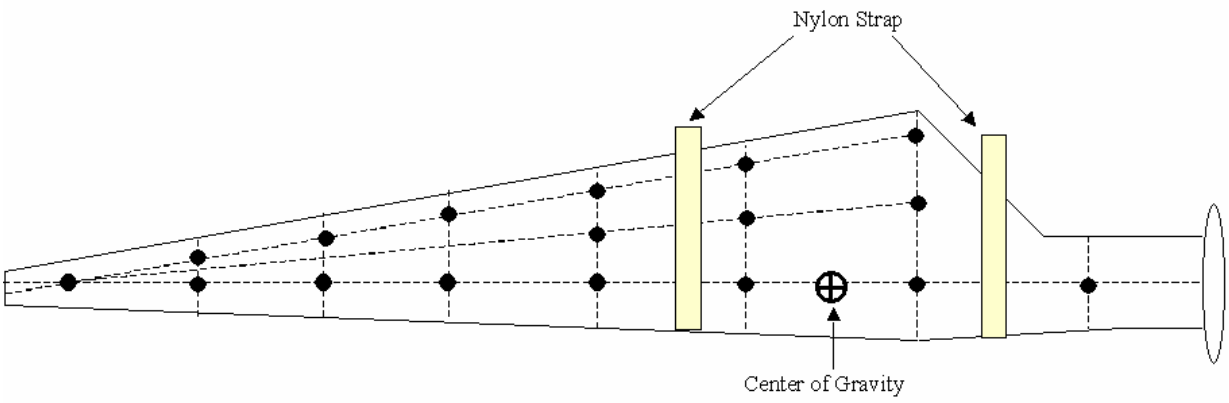

Figure C-17. Two-Nylon Strap Placement

When using a single nylon strap, it is positioned at the blade's CG. The blade may need to be lifted, lowered and then readjusted several times in order to test that the strap is indeed at the CG so the blade does not lean to one side. Please note that the marked CG may not be the ideal place to hang the blade as extraneous objects on the blade may cause a CG shift in either direction as seen in Figure C-18.

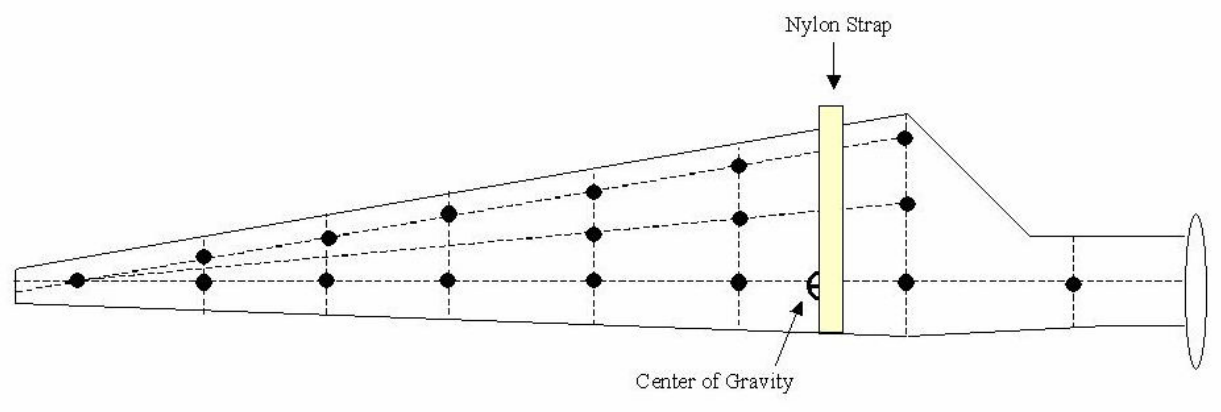

Figure C-18. One-Nylon Strap Placement

A bungee cord is then connected between the nylon strap(s) and the tripod(s) as seen in Figure C-19.

Figure C-19. Detailed view of the single-strap suspension system

During testing, the blade is to be lifted enough to free itself from its stands. The blade's stands are not to be removed in the instance that any support fails. A force input to the structure is produced using an instrumented three-pound hammer during modal testing. Several input locations are necessary to insure all the modes can be extradited. A log can help document file names, temperature, impact location, number of straps, etc. similar to Appendix E as will as data acquisition parameters, Appendix F.

Appendix D
Accelerometer Mounting Locations

Note that all measurements were taken with the implied Cartesian coordinate system's origin was located at the center of the respective blade's hub as described in the procedure, Appendix C.

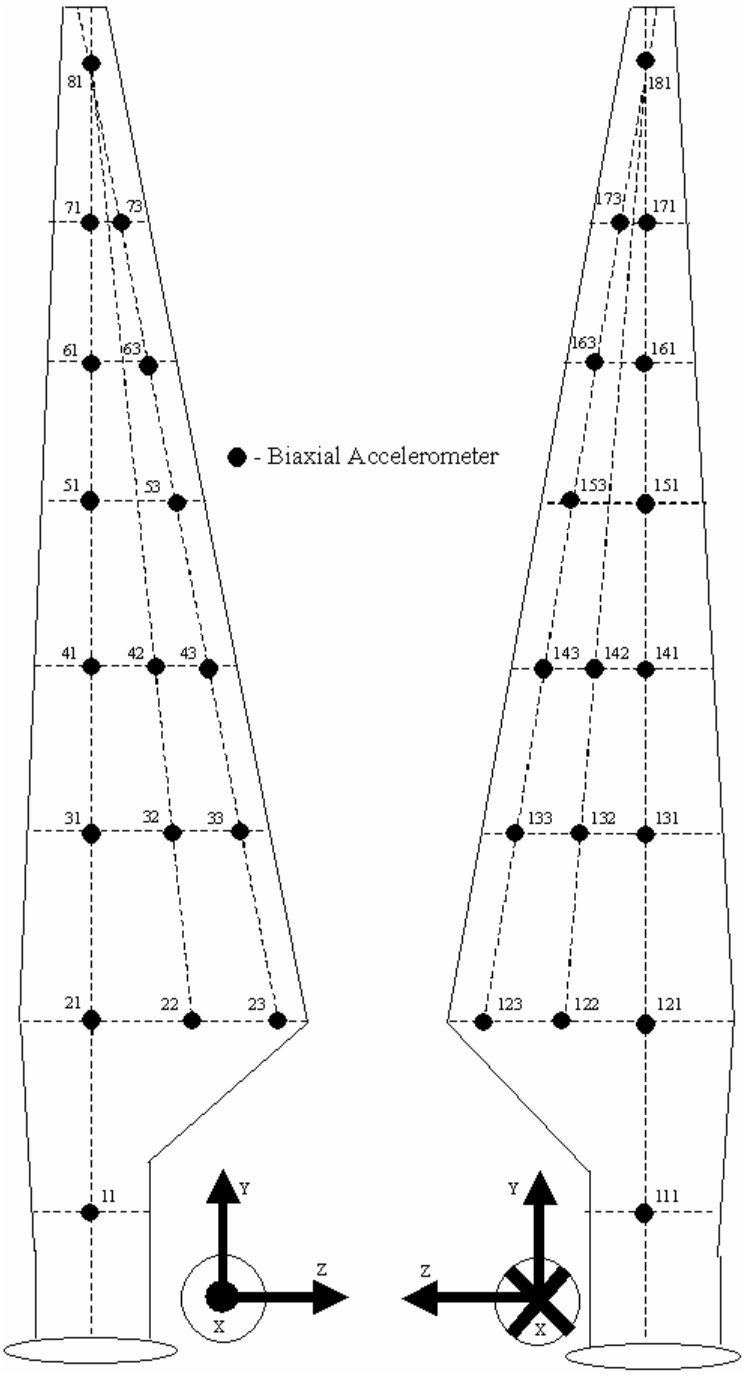

Figure D-1. Accelerometer Mounting Locations

Table D-1. Accelerometer Locations of Blade Serial #TX-100-001

Accelerometers		Coordinates		
Location	Meas. Axis	X (in)	Y (in)	Z (in)
11	X, Z	7	20.125	0
21	X, Z	6.125	68.625	-0.125
22	X, Z	5.125	68.5	12.5
23	X, Z	3.25	69	25
31	X, Z	6.25	115.375	-0.125
32	X, Z	5.125	115.375	10.125
33	X, Z	2.75	115.5	19.625
41	X, Z	6.375	161.125	-0.125
42	X, Z	5	161.25	7.5
43	X, Z	2.875	161.625	14.625
51	X, Z	6.625	209.25	-0.25
53	X, Z	3.75	209.5	11
61	X, Z	6.75	257.375	-0.25
63	X, Z	4.75	257.75	8
71	X, Z	6.75	305.425	-0.125
73	X, Z	5.75	305.425	3.75
81	X, Z	6.875	353.25	0.375
181	X, Z	5.75	353	0.375
171	X, Z	4.625	304.925	-0.25
173	X, Z	4.5	304.8	3.625
161	X, Z	3.375	256.375	-0.375
163	X, Z	3.5	256.25	7.375
151	X, Z	1.75	208.875	-0.375
153	X, Z	2.5	208.875	11.125
141	X, Z	0.125	161.25	-0.375
142	X, Z	1.375	161	7.75
143	X, Z	1.625	161	15.5
131	X, Z	-1.375	114.25	-0.25
132	X, Z	0.5	114.25	10.25
133	X, Z	1.375	113.75	20
121	X, Z	-4	66.75	0
122	X, Z	-0.875	66.5	12.75
123	X, Z	1.875	66.5	24.5
111	X, Z	-5	20.375	-0.125

Table D-1. Accelerometer Locations of Blade Serial #TX-100-003

Accelerometers		Coordinates		
Location	Meas. Axis	X (in)	Y (in)	Z (in)
11	X, Z	7.375	19.5	0.25
21	X, Z	6.5	69.75	1
22	X, Z	5.75	69.625	12.75
23	X, Z	3.5	69	25
31	X, Z	6.75	115.25	0.75
32	X, Z	5.25	115.25	11.125
33	X, Z	2.875	115.375	20
41	X, Z	6.75	162	0.75
42	X, Z	5.5	162.375	8.375
43	X, Z	3.25	162.75	15.375
51	X, Z	7	209.625	-0.125
53	X, Z	3.75	210.125	11
61	X, Z	7.125	257.25	0.5
63	X, Z	4.875	257.5	7.25
71	X, Z	7.125	304.75	0.25
73	X, Z	5.625	304.875	4
81	X, Z	7.625	352.25	0.75
181	X, Z	6.625	352.75	0.375
171	X, Z	5	304.625	0
173	X, Z	4.375	304.625	3.625
161	X, Z	3.625	256.5	0
163	X, Z	3.625	256.875	7.5
151	X, Z	1.9375	209.25	-0.25
153	X, Z	2.5625	209.625	11
141	X, Z	0.375	161.75	0.375
142	X, Z	1.8125	162	8.375
143	X, Z	2	162.25	15.25
131	X, Z	-1.25	115	0.75
132	X, Z	0.5625	115	10.5
133	X, Z	1.875	115	19.375
121	X, Z	-3.5	67.75	1.5
122	X, Z	-0.375	67.75	12
123	X, Z	2.125	67.75	24.25
111	X, Z	-5.375	19.625	0.125

Distribution

James Ahlgrimm
Office of Wind and Hydropower Technologies
EE-2B Forrestal Building
U.S. Department of Energy
1000 Independence Avenue SW
Washington, DC 20585

Mike Bergey
Bergey Wind Power Company
2200 Industrial Blvd.
Norman, Ok 73069

Derek Berry
TPI Composites, Inc.
373 Market Street
Warren, RI 02885-0328

Gunjit Bir
NREL/NWTC
1617 Cole Boulevard
Golden, CO 80401

C. P. Sandy Butterfield
NREL/NWTC
1617 Cole Boulevard
Golden, CO 80401

Garrett Bywaters
Northern Power Systems
182 Mad River Park
Waitsfield, VT 05673

Jack Cadogan
Office of Wind and Hydropower Technologies
EE-2B Forrestal Building
U.S. Department of Energy
1000 Independence Avenue SW
Washington, DC 20585

Doug Cairns
Montana State University
Department of Mechanical & Industrial
Engineering
College of Engineering
P.O. Box 173800
Bozeman, MT 59717-3800

David Calley
Southwest Windpower
1801 West Route 66
Flagstaff, AZ 86001

Stan Calvert
Office of Wind and Hydropower Technologies
EE-2B Forrestal Building
U.S. Department of Energy
1000 Independence Avenue SW
Washington, DC 20585

Jamie Chapman
Texas Tech University
Box 41023
Lubbock, TX 79409-1023

Craig Christensen, Vice President
GE Wind
13681 Chantico Road
Tehachapi, CA 93561

R. Nolan Clark
USDA - Agricultural Research Service
P.O. Drawer 10
Bushland, TX 79012

C. Jito Coleman
Northern Power Systems
182 Mad River Park
Waitsfield, VT 05673

S. Finn
GE Global Research
One Research Circle
Niskayuna, NY 12309

Peter Finnegan
GE Global Research
One Research Circle
Niskayuna, NY 12309

R. Gopalakrishnan
GE Wind Energy
GTTC, 300 Garlington Road
Greenville, SC 29602

Dayton Griffin
Global Energy Concepts, LLC
5729 Lakeview Drive NE, Ste. 100
Kirkland, WA 98033

Craig Hansen
Windward Engineering
2225 E. Murray-Holladay Rd. #201A
Salt Lake City, UT 84117

Jim Heath
Entegrity Wind Systems
PO Box 832
Charlottetown, PE C1A 7L9
Canada

Thomas Hermann
Wetzel Engineering, Inc.
P.O. Box 4153
Lawrence, KS 66046-1153

William E. Holley
GE Wind Energy
GTTC, M/D 100D
300 Garlington Rd., P.O. Box 648
Greenville, SC 29602-0648

Adam Holman
Alternative Energy Institute
West Texas A & M University
USDA-Agricultural Research Service
Conservation & Production Research
Laboratory
P.O. Drawer 10
Bushland, TX 79012-0010

Scott Hughes
NREL/NWTC
1617 Cole Boulevard, MS 3911
Golden, CO 80401

Kevin Jackson
Dynamic Design
123 C Street
Davis, CA 95616

Eric Jacobsen
GE Wind Energy
GTTC, 300 Garlington Road
Greenville, SC 29602

Gary Kanaby
Knight & Carver Yacht Center
1313 Bay Marina Drive
National City, CA 91950

Steve Lockard
TPI Composites, Inc.
373 Market Street
Warren, RI 02885-0367

James Locke
Wichita State University
207 Wallace Hall, Box 44
Wichita, KS 67260-0044

David Malcolm
Global Energy Concepts, LLC
5729 Lakeview Drive NE, Ste. 100
Kirkland, WA 98033

John F. Mandell
Montana State University
302 Cableigh Hall
Bozeman, MT 59717

Tim McCoy
Global Energy Concepts, LLC
5729 Lakeview Drive NE, Ste. 100
Kirkland, WA 98033

Amir Mikhail
Clipper Windpower Technology, Inc.
6305 Carpinteria Ave. Suite 300
Carpinteria, CA 93013

Walt Musial
NREL/NWTC
1617 Cole Boulevard
Golden, CO 80401

NWTC Library (5)
NREL/NWTC
1617 Cole Boulevard
Golden, CO 80401

Byron Neal
USDA - Agricultural Research Service
P.O. Drawer 10
Bushland, TX 79012

Steve Nolet
TPI Composites, Inc.
373 Market Street
Warren, RI 02885-0328

Richard Osgood
NREL/NWTC
1617 Cole Boulevard
Golden, CO 80401

Tim Olsen
Tim Olsen Consulting
1428 S. Humboldt St.
Denver, CO 80210

Robert Z. Poore
Global Energy Concepts, LLC
5729 Lakeview Drive NE
Suite 100
Kirkland, WA 98033

Michael Robinson
NREL/NWTC
1617 Cole Boulevard
Golden, CO 80401

Daniel Sanchez
U.S. Department of Energy
NNSA/SSO
P.O. Box 5400 Mail Stop: 0184
Albuquerque, NM 87185-0184

Scott Schreck
NREL/NWTC
1617 Cole Boulevard
Golden, CO 80401

Brian Smith
NREL/NWTC
1617 Cole Boulevard
Golden, CO 80401

Robert W. Thresher
NREL/NWTC
1617 Cole Boulevard
Golden, CO 80401

Case P. van Dam
Dept. of Mechanical & Aerospace Eng.
University of California, Davis
One Shields Avenue
Davis, CA 95616-5294

Jeroen van Dam
Windward Engineering
NREL/NWTC
1617 Cole Boulevard
Golden, CO 80401

Kyle Wetzel
Wetzel Engineering, Inc.
PO Box 4153
Lawrence, KS 66046-1153

Mike Zuteck
MDZ Consulting
601 Clear Lake Road
Clear Lake Shores, TX 77565

M.S. 0557	T. J. Baca, 1523
M.S. 0847	J. M. Redmond, 1526
M.S. 0843	J. Pott, 1524
M.S. 0847	P. J. Wilson, 1520
M.S. 0557	T. G. Carne, 1525
M.S. 0557	T. W. Simmermacher, 1523
M.S. 0557	D. T. Griffith, 1523
M.S. 0708	P. S. Veers, 6214
M.S. 0708	T. D. Ashwill, 6214 (10)
M.S. 0708	D. E. Berg, 6214
M.S. 0708	P. L. Jones 6214
M.S. 0708	D. L. Laird, 6214
M.S. 0708	D. W. Lobitz, 6214
M.S. 0708	J. Paquette, 6214
M.S. 0708	M. A. Rumsey, 6214
M.S. 0708	J. R. Zayas, 6214
M.S. 1245	M. Donnelly, 02453
M.S. 0612	A. M. Lucero, 04532
M.S. 0899	Technical Library, 9616 (2)
M.S. 9018	Central Technical Files, 8944